NOVA SCHOOL OF SCIENCE & TECHNOLOGY

DEPARTMENT OF MATERIALS SCIENCE

DAVID FERNANDES GRANJA

Bachelor of Sciences in Micro and Nanotechnology Engineering

NANOSTRUCTURED ELECTRODES FOR MICROSUPERCAPACITORS

MASTER IN MICRO AND NANOTECHNOLOGY ENGINEERING

NOVA University Lisbon

September, 2023

DEPARTMENT OF MATERIALS SCIENCE

NANOSTRUCTURED ELECTRODES FOR MICROSUPERCAPACITORS

DAVID FERNANDES GRANJA

Bachelor of Sciences in Micro and Nanotechnology Engineering

Adviser: Dr. Joana Dória Vaz Pinto
Associate Professor, NOVA University Lisbon

Co-adviser: Dr. João Carlos Mesquita Coelho
Researcher, CENIMAT|I3N, NOVA University Lisbon

Examination Committee:

Chair: Dr. Rui Alberto Garção Barreira do Nascimento Igreja,
Associate Professor, FCT-NOVA

Rapporteur: Dr. Ana Catarina Bernardino Baptista,
Senior Researcher, FCT-NOVA

Adviser: Dr. João Carlos Mesquita Coelho,
Researcher, FCT-NOVA

MASTER IN MICRO AND NANOTECHNOLOGY ENGINEERING

NOVA University Lisbon
September, 2023

Nanostructured Electrodes For Microsupercapacitors

ACKNOWLEDGMENTS

First, I would like to thank my supervisor, Dr. Joana Vaz Pinto, and my co-supervisor, Dr. João Coelho for their enormous support, colossal patience, and constant availability throughout this intellectually stimulating yet taxing journey. Thank you also for the understanding on a more personal matter when I was going through a less good period, you tried to push me and motivate to achieve good results. Without you this work would not be made possible.

Second, I express my deep gratitude to the entire team at the Department of Material Sciences (DCM) and CENIMAT|i3N, as well as the professors at DCM, for their support during my academic journey. A special thanks goes to Ricardo Correia for his help and guidance during the initial stages of lab experiments that would later lead to the ground floor of my thesis. I am also grateful for the opportunity to use the lab equipment to create structures and perform essential characterizations that led to the conclusions in my work.

Last but not least, I extend my heartfelt gratitude to my family, my father, my mother, my friends and my girlfriend for their love, sacrifices, unwavering support and forbearance, which were crucial in my personal development. I am thankful as well for the priceless teachings and values they have instilled upon me.

"If I have seen further it is by standing on the shoulders of giants."

Isaac Newton

ABSTRACT

The demand for miniaturized energy storage solutions has grown exponentially in recent years, driven by the proliferation of portable electronics, wearable devices, and the advent of the Internet of Things (IoT). Microsupercapacitors, with their rapid charge/discharge capabilities and long cycle life-times, have emerged as promising candidates for meeting these energy storage needs. This thesis ex-plores a methodology to further enhance the performance of microsupercapacitors by electrodepositing nanostructured MnO_2 films onto gold current collectors. In a photolithographic process, interdigital pla-nar electrodes were created, and their spacing was investigated for its impact on device performance, revealing no significant influence. In an attempt to texturize the electrode surface, the electrodeposition process was optimized for MnO_2 film growth at deposition times below 5 min and a high electrodepo-sition potential of 0.95 V. A solution of Mn_2SO_4 (0.15 M) and Na_2SO_4 (0.1 M) was used in the electro-deposition process, with the deposition lasting for a duration of 2 minutes, resulting in a film thickness of 1.8 ± 0.2 µm and a specific capacitance of 18 ± 2 mF/cm². Raman spectroscopy and XRD confirmed an amorphous MnO_2 character, with hints of $Ca_{0.8}Mn_8O_{16}$ polycrystalline aggregates. The film exhibited thickness variation within a range of ± 0.2 µm and porous nanostructures. Different gel electrolytes were tested, with PVA/LiCl performing best due to compatibility with the active material. The final interdigitated MicroSupercapacitor (MSC) iteration exhibited a capacitance of 48.70 ± 0.04 µF/cm² (at a current density of 0.24 µA/cm²) for Au electrodes without MnO_2 and 2.4 ± 0.6 mF/cm² (at a current density of 11.9 µA/cm²) with MnO_2, indicating a significant increase in both capacitance and current density with the addition of MnO_2. To create flexible MSCs, the fabrication process was adapted for a parylene-C film substrate with 11.5 ± 1.5 µm thickness, resulting in a flexible interdigitated MSC with MnO_2 showing a capacitance of 0.6 ± 0.1 mF/cm² (at a current density of 2.93 µA/cm²).

Keywords: Microsupercapacitor; Electrode deposition; Manganese Oxide

RESUMO

A procura de soluções miniaturizadas de armazenamento de energia tem crescido exponencialmente nos últimos anos, impulsionada pela proliferação de eletrónica portátil, dispositivos portáteis e o advento da Internet das Coisas (IoT). Os micro-supercondensadores (MSC) com as suas capacidades de carga/descarga rápida e ciclos de vida longos, surgiram como candidatos promissores para satisfazer estas necessidades de armazenamento de energia. Esta tese explora uma metodologia para melhorar ainda mais o desempenho dos micro-supercondensadores através da eletrodeposição de filmes optimizados de MnO_2 nanoestruturados nos seus colectores de corrente de ouro. Num processo fotolitográfico, foram criados eléctrodos planares interdigitais e o seu espaçamento foi investigado quanto ao seu impacto no desempenho do dispositivo, não revelando qualquer influência significativa. Numa tentativa de texturizar a superfície do elétrodo, o processo de eletrodeposição foi optimizado para o crescimento do filme de MnO_2 com tempos de deposição inferiores a 5 min e um elevado potencial de eletrodeposição de 0.95 V. Uma solução de Mn_2SO_4 e Na_2SO_4 foi utilizada no processo de eletrodeposição, com a deposição a durar 2 minutos, resultando num filme com uma espessura de 1.8 ± 0.2 μm e uma capaci-dade específica de 18 ± 2 mF/cm². A espetroscopia Raman e o XRD confirmaram um carácter amorfo do MnO_2, com indícios de agregados policristalinos de $Ca_{0.8}Mn_8O_{16}$. O filme apresentou variação de espessura dentro de uma faixa de ± 0.2 μm e nanoestruturas porosas. Foram testados diferentes electró-litos em gel, sendo que o PVA/LiCl teve o melhor desempenho devido à compatibilidade com o material ativo. A iteração final do micro-supercondensador interdigitado apresentou uma capacidade de 48.70 ± 0.04 μF/cm² (a uma densidade de corrente de 0.24 μA/cm²) para eléctrodos de Au sem MnO_2 e 2.4 ± 0.6 mF/cm² (a uma densidade de corrente de 11.9 μA/cm²) com MnO_2, indicando um aumento significativo da capacidade e da densidade de corrente com a adição de MnO_2. Para criar MSCs flexíveis, o processo de fabrico foi adaptado a um substrato de película de parileno-C com 11.5 ± 1.5 μm de espessura, resultando num MSC interdigitado flexível com MnO_2 que apresenta uma capacitância de 0.6 ± 0.1 mF/cm² (a uma densidade de corrente de 2.93 μA/cm²).

Palavras-chave: Micro-supercondensadores; Deposição de eléctrodos; Óxido de manganês

CONTENTS

ACKNOWLEDGMENTS I

ABSTRACT III

RESUMO IV

LIST OF FIGURES VII

LIST OF TABLES IX

ACRONYMS XI

SYMBOLS XIII

1 INTRODUCTION 1

2 MATERIALS AND METHODS 5

2.1 Interdigital Electrode Fabrication 5

2.2 Electrodeposition of MnO_2 6

2.3 Films characterization 6

2.4 Electrochemical Characterization 6

3 RESULTS AND DISCUSSION 8

3.1 Evaluation of interdigital spacing on device performance 8

3.2 Manganese oxide electrodeposition 11

3.2.1 Structural and Morphological Characterization of MnO_2 14

3.3 Gel Electrolyte Testing 18

3.3.1 Electrolyte performance comparison 18

3.3.2 Gel electrolyte compatibility evaluation 19

3.4 MSCs: Fabrication and Electrochemical Characterization 20

3.4.1 Assembly and Characterization of Flexible MSCs 23
3.4.2 Flexible MSC Performance Analysis and Comparison 25
4 CONCLUSIONS AND FUTURE PROSPECTS 29

LIST OF FIGURES

Figure 1- Scheme of (a) an electric double-layer capacitor and (b) a pseudocapacitor. Adapted from [5]..... 2

Figure 2.1- Photomasks used in the production of the interdigitated electrodes in a) and b) and in c) the electrochemical setup used to electrodeposit the MnO_2. 5

Figure 3.1- Geometry of the MSC interdigitated electrode..... 8

Figure 3.2 - CV test on the Interdigitated electrode design with finger interspacing distance of 400 µm..... 9

Figure 3.3- Specific capacitance by Scan rate test on the interdigitated MSC designs: 100 µm, 200 µm, 400 µm, and 600 µm. 10

Figure 3.4- MnO_2 film samples produced in a 5 min electrodeposition from the precursor solutions: Manganese acetate ($Mn(CH_3COO)_2$) (left side); Manganese sulfate ($MnSO_4$) (right side). 11

Figure 3.5- Film thickness versus respective electrodeposition time. 12

Figure 3.6- Electrodeposited MnO_2 samples obtained at deposition intervals of 60 s, ranging from 1 to 5 min (left to right). 12

Figure 3.7- Specific areal capacitance versus film thickness, calculated @ 5 mV/s Scan rate (left side); @ 30 mV/s Scan rate (right side). 13

Figure 3.8- X-ray diffractograms (left) and Raman spectra (right) of MnO_2 films produced by $MnSO_4$ (Sulfate) and $Mn(CH_3COO)_2$ (Acetate) precursor solutions. 15

Figure 3.9- SEM images of the MnO_2 film: Border of the electrodeposited region (30x magnification) (left); Central region of the film (30x magnification) (middle); Zoom In on the central region of the film (500x magnification) (right). 16

Figure 3.10- Optical microscopy images of the MnO_2 film: Border region of the deposition zone (left); Central region of the film (right). 17

Figure 3.11- Specific capacitance comparison between PVA/LiCl and PVA/H_2SO_4 across all measured scan rates for a 600 µm interdigitated electrode. 18

Figure 3.12- Gel electrolytes drop casted onto MnO2 samples- a) PVA/LiCl; b) PVA/H_2SO_4; c) PVA/H3PO4; d) None (control sample). 19

Figure 3.13- Schematic illustration for the fabrication processes of the MSCs..... 20

Figure 3.14- CV test on the interdigitated MSC's: without MnO_2 (left) and with MnO_2 (right). 21

Figure 3.15- Specific capacitance by current density test on the interdigitated MSC without MnO_2 (left plot) and with MnO_2 (right plot). 22
Figure 3.16- Flexible Interdigitated MSC with optimized MnO_2 thin film. 24
Figure 3.17- CV test on the flexible interdigitated MSC with MnO_2. 24
Figure 3.18- CV scan comparison for the produced MSC variants, displayed at a singular Scan rate of 5 V/s. 26
Figure 3.19- Specific capacitance comparison between MSC variants across all measured scan rates. 26

LIST OF TABLES

Table 1- Geometric features of each electrode design. 9
Table 2- Comparison of Specific areal capacitance values obtained for each electrode design: @ 5 mV/s Scan rate; @ 30 mV/s Scan rate. 10
Table 3- Summary table of obtained electrodeposition data. 13
Table 4- Summary table of obtained MSC specific capacitance and energy density. 27

ACRONYMS

a.u	Arbitrary units
MSC	Micro supercapacitor
EDL	Electric double-layer
EDLC	Electric double-layer capacitor
WE	Working electrode
CE	Counter electrode
RE	Reference electrode
CV	Cyclic voltammetry
EIS	Electrochemical impedance spectroscopy
GCD	Galvanostatic charge-discharge
LIB	Lithium-ion battery
PVA	Polyvinyl alcohol
SEM	Scanning Electron Microscopy
XRD	X-ray diffraction
XPS	X-ray Photoelectron Spectroscopy
EIS	Electrochemical Impedance Spectroscopy
EDS	Energy-dispersive X-ray Spectroscopy
DC	Direct current

SYMBOLS

C_A	Specific areal capacitance
A	Integrated absolute area of a cyclic voltammogram
v	Scan rate
ΔV	Voltage window
a	Area in cm^2
I	Electric current
E_D	Energy density

1

INTRODUCTION

The growing interest in portable and wearable technologies has incited the demand for enhanced energy storage and harvesting systems [1], [2]. Although lithium-ion batteries (LIBs) are widely utilized, they face challenges in miniaturization, rely on potentially hazardous electrolytes, and depend on lithium, a scarce resource. Microsupercapacitors (MSCs) emerge as a promising solution for such applications, showcasing remarkable attributes like high power density, extended lifespan, rapid charge-discharge capabilities, and straightforward designs [1]–[3]. Specifically, a planar interdigitated MSC configuration can be adapted to yield flexible, lightweight, and easily packaged devices, a departure from conventional metal-based sandwich structures [1]–[5]. Furthermore, MSCs can seamlessly integrate into systems, serving as standalone units or complementing other energy storage solutions [6].

Supercapacitors can be generally categorized into two types based on their charge storage mechanisms: electric double-layer capacitors (EDLCs) and pseudocapacitors. EDLCs store energy by means of electrostatic forces, creating charges around the electrolyte ions at the electrode-electrolyte interface, a phenomenon often described using the Gouy-Chapman-Stern model [5], [7]. This physical process, involving non-faradaic charge transfer, is reversible at remarkably high rates and can achieve a high power density. However, the energy density is relatively smaller because of the inherent limitations of the electrostatic charge transfer mechanism and its physical properties. Figure 1a depicts a simplified scheme of an EDLC.

In contrast, pseudocapacitors leverage rapid and reversible surface redox processes involving active electrode materials like conductive polymers or metal oxides. This enhances the charge storage capacity but comes at the cost of decreased power output and cycling durability for the device [8], [9]. Figure 1b depicts a simplified scheme of the pseudocapacitive mechanism.

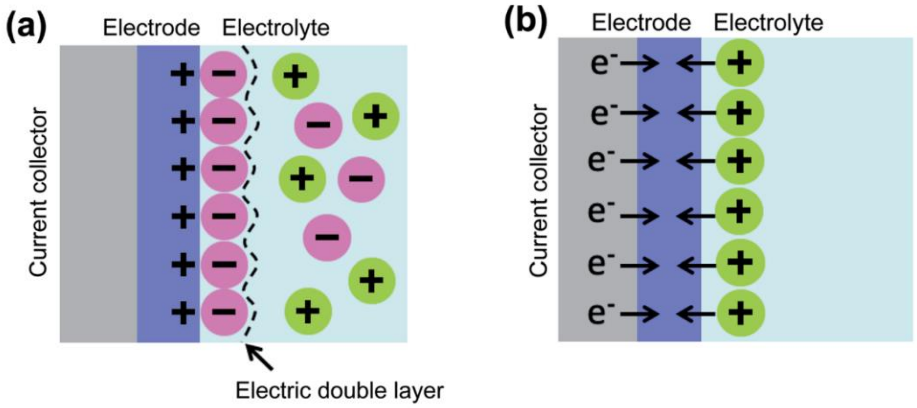

Figure 1- Scheme of (a) an electric double-layer capacitor and (b) a pseudocapacitor. Adapted from [5].

As it results from Figure 1 the main components of a supercapacitor are the electrodes, the corresponding current collectors, a separator (or electrode material) between them, and an electrolyte. For this application, the electrolyte usually takes the form of either a liquid solvent or a solid-state or quasi-solid-state substance [6], [10]. Typically, MSC electrolytes are polymer-based, consisting of an acid (H_2SO_4) [11], a neutral salt (LiCl) [12], or a base (KOH) [13], dissolved within aqueous polyvinyl alcohol (PVA) matrices.[6] This approach offers a straightforward and cost-effective method for MSC fabrication. Nevertheless, it is worth noting that water-based systems have a relatively limited voltage window [6], [10], [14].

When it comes to fabricating interdigitated current collectors, various authors, including Velasco, Zhang, Zheng, and Liu et at.[5], [14]–[18], have made noteworthy observations and shared valuable insights regarding the utilization of photolithography for this purpose. Despite its downsides, photolithography remains one of the best methods for achieving patterned, high-quality thin film electrodes. This technique has proven to be effective in fabricating intricate structures for various applications, particularly in the field of electrochemistry and microelectronics [18]. Gold is usually used as an electrode material, as it is a highly stable material with exceptional qualities that make it an ideal choice for use as the material in the MSC's current collectors [16]. Its stability and inertness in various electrochemical environments prevent corrosion and reactions with a wide range of chemicals, making it suitable for diverse experimental conditions. Additionally, gold's high conductivity facilitates efficient electron transfer between the electrode surface and the electrolyte solution, essential for fast and accurate electrochemical measurements. Moreover, gold electrodes can be easily functionalized with surface modifications, allowing researchers to tailor surface properties to achieve enhanced desired characteristics [15], [16]. Furthermore, gold interdigital MSC electrodes can be manufactured with high precision and reproducibility, ensuring consistent results in electrochemical experiments [16]. These attributes collectively make gold an excellent current collector material for studying, assessing, and benchmarking the electrochemical properties of functionalized electrode surfaces effectively.

When assessing the electrochemical capabilities of a material for potential electrode use, as opposed to evaluating the overall supercapacitor performance, measurements are conducted using a three-electrode setup. In this configuration, the system comprises a reference electrode for precisely pinpointing potentials against a well known reference potential, a counter electrode, and the electrode under investigation serving as the working electrode. All these components are immersed in an aqueous electrolyte.

Regarding electrodes active material, manganese dioxide (MnO_2), often referred to as manganese oxide, is a pseudocapacitive material that demonstrates significant potential for enhancing the electrochemical performance of MSCs [16]. MnO_2 proves to be an appealing choice for supercapacitor electrodes, thanks to its favorable attributes such as high energy and power density, excellent specific capacitance, affordability, and eco-friendliness [16], [19]. From several methodologies to deposit/grow metal oxides onto the Interdigitated electrodes, electrodeposition is one of the simplest and most effective [20]. In short, this technique utilizes a three-electrode electrodeposition setup in which voltage or current is applied between the working electrode and the counter electrode, leading to electrochemical reactions occurring at the surface of the working electrode. The reference electrode plays a crucial role in maintaining a constant potential at the working electrode, thereby ensuring precise control over the deposition process. In contrast to alternative techniques employed for the deposition of transition metal oxides, electrodeposition showcases several advantages. These include facile mass control, excellent conductivity, homogenous depositions, and precise control of the oxidative/ reductive reactions [16], [20]. Consequently, the majority of research efforts focus on the three-electrode method to perform potentiostatic, galvanostatic or potentiodynamic depositions [16].

Zhang et al. [16] documented a MnO_2 potentiostatic electrodeposition using an aqueous solution containing 0.05 M $Mn(CH_3COO)_2/Na_2SO_4$, employing a three-electrode setup under a constant deposition potential of 0.45 V. These settings produced films with an areal capacitance of up to 3.29 $mF.cm^{-2}$ (based on the total footprint of the device) from a 30-minute plating time interval. Samples were registered, showing plating times ranging from 2 to 30 minutes, with respective current densities ranging from 0.0056 to 0.2778 mA/cm^2. Electroplated MSC samples were obtained by employing interdigitated gold electrodes, thereby producing symetric MSCs. In a similar approach, Wang et al. [21] used electrodeposited MnO_2 films as an anode material in in-plane asymmetric microsupercapacitors. These devices displayed a maximum areal specific capacitance of 13 mF/cm^2 (at a current density of 0.25 mA/cm^2), energy density of 5.88 $\mu Wh/cm^2$ (at a current density of 0.25 mA/cm^2) and a power density of 1.13 mW/cm^2. Additionally, Han et al. [22] reported that a MnO_2 electrodeposition in MSC electrodes resulted in an areal capacitance of up to 7.1 mF/cm^2 (at a current density of 0.02 mA/cm^2).

The enhanced electrochemical performance of MSCs functionalized with MnO_2 can be attributed to several factors. First, MnO_2 serves as a pseudocapacitive material, allowing it to store charge through reversible redox reactions. Additionally, the surface texturization increases the available active surface area for these redox reactions to take place. This phenomena, along with the double-layer capacitance provided by the interdigitated configuration of MSCs, result in a higher total capacitance compared to MSC's with gold interdigitated electrodes alone [22]–[24].

However, the literature on the electrodeposition of MnO_2 nanostructured thin films for interdigitated MSC electrodes is both sparse and outdated. Documentation for an updated iteration of this methodology, which includes low MnO_2 mass loading aiming for a thin film approach, rapid deposition times, and optimized film properties, is not readily available. While there are some works that document similar aspects, none of them provide information on the electrodeposition rate of the film under specific conditions, the specific areal capacitance of the films at various thicknesses within short

deposition time intervals, characterization on the quality of the produced films, or the thin-film-optimized implementation for interdigitated planar electrodes.

In this thesis it is explored a methodology for the production of microsupercapacitor electrodes, based on the electrodeposition of optimized nanostructured MnO_2 thin films as a means to texturize and functionalize the electrode's surface. By taking this approach, we aim to obtain higher specific areal capacitance, energy density, and current densities while employing minimal active material mass loadings.

As a consequence of this endeavour, we will undertake an assessment of the deposition process to estimate the electrodeposition rate of the MnO_2 film and determine the optimal film thickness for enhanced performance. Furthermore, we will conduct a comprehensive investigation into the structure and composition of the produced film, utilizing various analytical characterization methods. The MSC's gold interdigitated planar current collectors will undergo evaluation by testing different interdigital spacing configurations created through photolithography. Additionally, we will explore various electrolytes to identify the most suitable candidate for further implementation. To showcase the versatility of the developed approach, we will also produce a flexible MSC incorporating MnO_2 thin films.

2

MATERIALS AND METHODS

In this section, the methodology adopted for MSC fabrication and further process tunning is described.

2.1 Interdigital Electrode Fabrication

The fabrication of the Interdigital electrodes (IDE) was performed on 10x10 cm corning glass substrates, thoroughly cleaned in acetone, isopropanol and deionized water baths. The IDE patterns were produced by means of standard contact photolithography with the photomasks shown in figure 2.1a) and 2.1b). A positive photoresist (AZ 6632) was used and samples were exposed on a Suss MA45 UV mask aligner. AZ 726 MIF Developer was used to selectively remove the resist. After patterning the substrate, an 8 nm Ti film followed by an 85 nm Au film were deposited via E-beam evaporation using a homemade e-beam setup. Additionally, a lift-off process was performed on acetone to strip the remaining resist.

Parylene–C (Dichloro-p-cyclophane) deposited by CVD was used as a mask layer to layer to delimit the interdigital cathode and anode exposed areas, 2 g of parylene-C dimer were used on a PDS-2010 Labcoater 2 (Specialty Coating Systems) achieving a final thickness of near 1 µm. To expose the interdigital electrodes, Reactive Ion Etching (RIE) was used to etch the parylene film on a Trion Phantom 3 reactive ion etcher under O_2 atmosphere (O_2 flow of 30 sccm) for 1200 s (P = 50 W; p = 20 mTorr). The photolitographic mask used to create the photoresit etch mask can be found in Figure 2.1b).

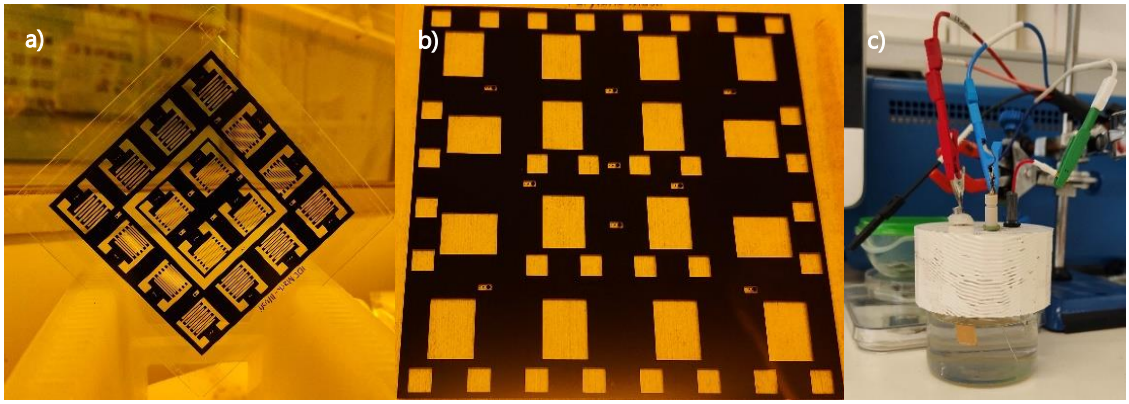

Figure 2.1- Photomasks used in the production of the interdigitated electrodes in a) and b) and in c) the electrochemical setup used to electrodeposit the MnO_2.

2.2 Electrodeposition of MnO_2

An electrodeposition custom setup was developed as shown in Figure 2.1c), using a 50ml round glass beaker and a custom 3D printed lid fitted to hold the working electrode (WE), the reference electrode (RE) (Ag/AgCl) , and the counter electrode (CE) (Pt). A BioLogic SP-50 potentiostat was used to perform the chronoamperometry experiments. Two aqueous solutions were tested: i) An acetate solution $Mn(CH_3COO)_2$ (0.05 M) + Na_2SO_4 (0.1 M); and ii) A sulphate solution, $MnSO_4$ (0.15 M) + Na_2SO_4 (0.1 M). Electrodeposition was carried out with chronoamperometry experiments with set potentials of -0.65 V vs Ag/AgCl for the acetate solution and -0.95 V vs Ag/AgCl for the sulfate solution.

2.3 Films characterization

The electrodeposited films and electrodes were characterized using various analytical characterization methods, summarized briefly as follows:

Raman Spectroscopy: Raman Spectroscopy was used to verify the presence of possible different phases of MnO_2 and measurements were taken in a Renishaw inVia Qontor micro-Raman spectrometer equipped with an air-cooled charge-coupled device (CCD) detector and an He–Ne laser operating at 50 mW, producing a 532 nm laser excitation. The laser intensity was set to 0.5 mW. An integration time of 3 scans of 10 s each was used for all measurements.

X-Ray Diffraction (XRD): Analysis was performed to ascertain the presence of crystalline phases, using an PANalytical X'Pert Pro MPD X-Ray diffractometer, with a Bragg−Brentano geometry (scan range of 2 θ from 15° to 90°) and Cu Kα line radiation (λ = 1.5406 Å).

Profilometry: Profilometry was used to acquire thickness measurements of the electrodeposited MnO_2 thin films. The measurements were taken in a Ambios XP-Plus 200 Stylus fitted with a diamond tipped stylus (2.5 micron tip radius). The horizontal scan length range was set to 90 mm.

Optical and Morphological characterization: The Morphological analysis of the MnO_2 covered Au/Ti electrodes was made using a Hitachi TM 3030Plus Tabletop SEM. The image acquisition was performed with an acceleration voltage of 15.0 kV, working distance of 10.90 mm and magnifications from 30× up to 1500×. Optical Microscopy was also used to obtain images of MnO_2 films and structures in a wider scale and were acquired with an Olympus BX51 Microscope fitted with a 3Mpixel camera and set to bright field mode.

2.4 Electrochemical Characterization

All the electrochemical characterization of both MSCs and electrodeposited MnO_2 samples was performed on a BioLogic SP-50 potentiostat. The three-electrode custom setup was employed, for analysis of the electrodeposited films: the cell was filled with 50 mL of (0.5 M) K_2SO_4 aqueous electrolyte and purged for 20 mins with nitrogen, before mounting the setup in the potentiostat. The WE consisted of a 1×1 cm delimited segment of the Au/Ti samples submerged in the electrolyte. For the MSCs analysis a standard two electrode setup was employed, connecting the CE and RE electrode to a MSC pad, and the WE to the other pad. To enhance electrical conductivity, silver Ink was applied to the MSC pads. All samples were characterized through cyclic voltammetry (CV) in a 0.0-0.9 V voltage window

and using 10 cycles for each scan rate, namely 5, 10, 30, 50, 100, 300, 500, 1000, 3000, 5000 and 10000 mV/s.

Four different electrolytes were tested, 1 aqueous and 3 gel electrolytes. The aqueous electrolyte was based on a 0.5 M K_2SO_4 solution prepared by simple dissolution. For the gel electrolytes, 1 g of PVA (average Mw 31.000-50.000) was dissolved in 10 ml of deionized water at 90 °C under vigorous stirring for 1 h. Then for each gel an acid or a neutral salt was added to complete the preparation.:

- **PVA/H_2SO_4 gel electrolyte**, 0.5 mL of H_2SO_4 (97%) was added to the PVA solution;
- **PVA/H_3PO_4 gel electrolyte**, 0.5 mL of H_3PO_4 (85%) was added to the PVA solution;
- **PVA/LiCl gel electrolyte:** 2.1g of LiCl (99%) was added to the PVA solution.

The electrolytes are then drop casted onto the devices over an area of ~1 cm^2 and left to dry overnight at room temperature.

3

RESULTS AND DISCUSSION

In this section, various electrodes configurations with distinct interdigital spacings were tested to evaluate whether the interdigital spacing distance is a significant parameter for enhancing device performance. An assessment of the MnO_2 deposition process was carried out to estimate the electrodeposition rate of the MnO_2 film and determine the optimal film thickness for enhanced performance. Additionally, a comprehensive investigation into the structure and composition of the produced film, utilizing various analytical characterization methods was performed. Electrolytes were evaluated for both performance and compatibility with the active material. Finally, MSCs were produced, and their electrochemical performance is evaluated. Additionally, to showcase the versatility of the developed approach, we will also produce a flexible MSC incorporating MnO_2 thin films.

3.1 Evaluation of interdigital spacing on device performance

Planar Interdigitated electrodes were produced using the production methods previously described in the Methods Section. These electrodes exhibit an aerial footprint of 1.75 cm length and 2.09 cm width as shown in Figure 3.1. The fingers dimensions were kept at 1.21 cm × 0.08 cm with a fixed interspacing distance.

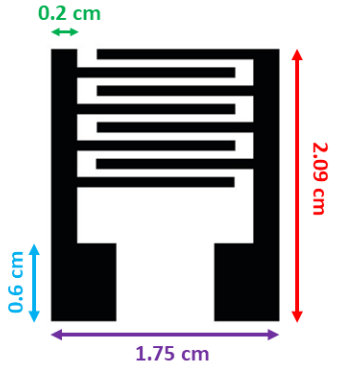

Figure 3.1- Geometry of the MSC interdigitated electrode.

The fixed interspacing distance varies for each photomask design. In total, four distinct designs were tested, with fixed finger interspacing distances of 100 µm, 200 µm, 400 µm, and 600 µm, respectively. For these electrodes, the device's areal footprint and the finger dimensions were kept the same but the finger's fixed interspacing distance and/or number of fingers was changed, meaning that for smaller Interspacing distances, the amount of finger was changed.

Table 1- Geometric features of each electrode design.

Electrode inter-spacing	100 µm	200 µm	400 µm	600 µm
Total finger active area Σ cm²	1.0176	0.9328	0.848	0.6784
Nº of fingers	12	11	10	8

To characterize the electrodes a PVA/H_2SO_4 gel electrolyte was drop casted onto the devices over a fixed area of ~1 cm^2. The samples were then characterized through cyclic voltammetry. The voltage window of 0.0-0.9 V was chosen due to the aqueous nature of the electrolytes, taking in to account the water electrolysis potential (1.23 V) [6], [14]. By comparing cyclic voltammograms of the 100, 200, 400, and 600 µm interspaced electrodes (Appendix A.1), no clear difference in the CV curves is observable, meaning that each sample presents a similar behaviour. All these CV curves present rhomboid-like shaped curves at low scan rates that become increasingly prominent at higher scan rates, as shown in Figure 3.2, a behaviour that is characteristic of non-ideal highly resistive capacitors. The absence of redox peaks also indicates that the samples are charged and discharged at a constant rate [25].

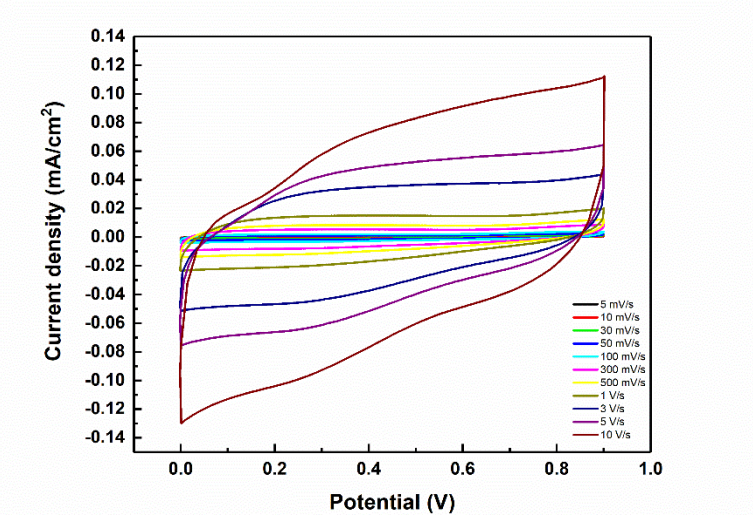

Figure 3.2- CV test on the Interdigitated electrode design with finger interspacing distance of 400 µm.

The specific areal capacitance, C_A, was calculated for each electrode configuration using Equation 1:

$$C_A = \frac{A}{2 \times v \times \Delta V \times a} \quad (1)$$

Where A is the integrated absolute area of a cyclic voltammogram, v is the scan rate, ΔV is the voltage window and a is the area of deposited active material.

C_A was calculated for each device at each measured scan rate. Through an analysis of the Figure 3.3 plot data, it is observed that there is a slight yet substantial disparity in C_A values at 5 mV/s for each configuration. However, this relative increase in disparity still falls under experimental error. For ease of comparison, it can be seen in Table 2 that, for instance, at a higher scan rate (30 mV/s), the similarity between C_A values of each configuration is more evident.

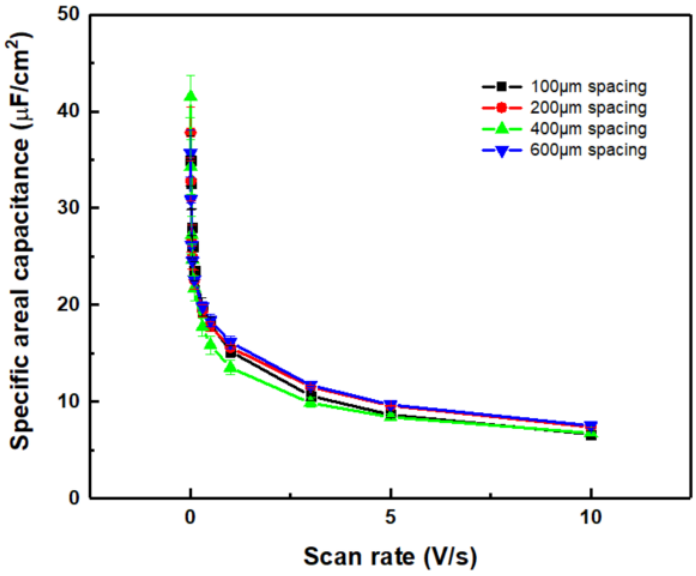

Figure 3.3- Specific capacitance by Scan rate test on the interdigitated MSC designs: 100 μm, 200 μm, 400 μm, and 600 μm.

Table 2- Comparison of Specific areal capacitance values obtained for each electrode design: @ 5 mV/s Scan rate; @ 30 mV/s Scan rate.

Electrode interspacing	C_A @ (5 mV/s Scan rate)	C_A @ (30 mV/s Scan rate)
100 μm	34.9 ± 2.3 μF/cm^2	28 ± 1.9 μF/cm^2
200 μm	37.8 ± 2.6 μF/cm^2	26.9 ± 1.4 μF/cm^2
400 μm	41.5 ± 2.2 μF/cm^2	27.2 ± 1.8 μF/cm^2
600 μm	35.6 ± 2.4 μF/cm^2	26.2 ± 1.3 μF/cm^2

Through the data, it is possible to ascertain that, for the electrode designs used, the interdigital spacing of the electrodes was not a significant parameter for device performance deterioration. This is due to the only real difference between electrodes being the available active area, and not geometric factors that influence the charge accumulation phenomena at the electrode's interface. Therefore, the electrode configuration with 600 μm of interdigital spacing was then used for further MSC device implementation. This particular configuration was chosen because, from a manufacturing perspective, it is the most easily reproducible.

3.2 Manganese oxide electrodeposition

To evaluate the electrodeposition process, various 2.5×1 cm Au/Ti electrodes were cut. The immersed deposition area was set to 1 cm^2. Two distinct aqueous solutions, each with their respective chronoamperometric potentials, were evaluated for use in deposition baths. The first solution consisted of $Mn(CH_3COO)_2$ with Na_2SO_4, (referred as acetate solution) which was electrodeposited at -0.65 V vs Ag/AgCl. The second solution consisted of $MnSO_4$ with Na_2SO_4, (referred as sulfate solution) electrodeposited at -0.95 V vs Ag/AgCl. The electrodeposition was carried out in a three-electrode setup, following the methodology and described in Zhang et al. [16]. Several electrodeposition time intervals were tested, the most promising samples were obtained from time intervals up to 5 minutes, samples that surpassed that time interval were deemed non usable due to irregular film deposition and uneven oxide film thickness along the electrode area upon visual inspection. For samples within the 5-minute interval, the films exhibited a greater level of homogeneity, but the resulting material still exhibited undesirable traits, such as poor adhesion, fragility, and brittleness (Figure 3.4- left side).

In order to produce higher quality MnO_2 films, an alternative was evaluated. According to Yi et al. [20], an aqueous solution of $MnSO_4$ with Na_2SO_4 in an electrodeposition at -0.95 V (DC) would provide a viable alternative. At preliminary testing, these films (Figure 3.4 - right side) appear to visually present an excellent homogenous and uniform oxide deposition unlike samples produced with the previous settings. The oxide films were then produced for electrodeposition time intervals ranging from 1 to 5 min (in 60 s deposition intervals) and then further characterized (Figure 3.6).

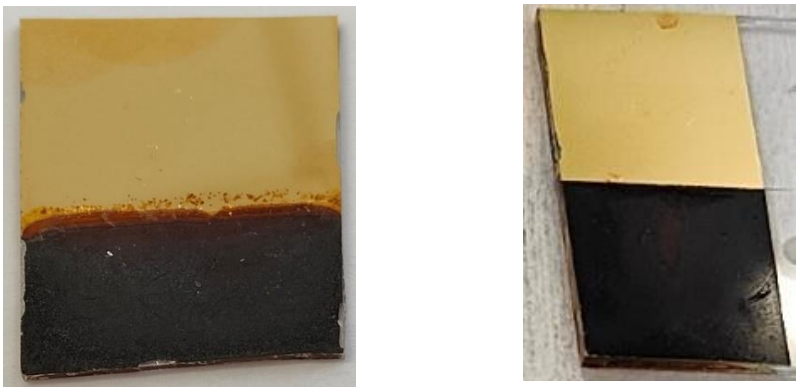

Figure 3.4- MnO_2 film samples produced in a 5 min electrodeposition from the precursor solutions: Manganese acetate ($Mn(CH_3COO)_2$) (left side); Manganese sulfate ($MnSO_4$) (right side).

Thickness measurements of the oxide films were acquired through profilometry. In total, six sample replicas were made for each time interval of deposition, each measurement was then repeated three times for each sample. The collected data is shown in Figure 3.5. As observed, the deposition followed an apparent linear deposition rate after the first minute for the contemplated timespan of depositions. An estimate of the MnO_2 deposition rate was calculated by taking plot data from Figure 3.5, resulting in an estimate of ~0.4 μm/min.

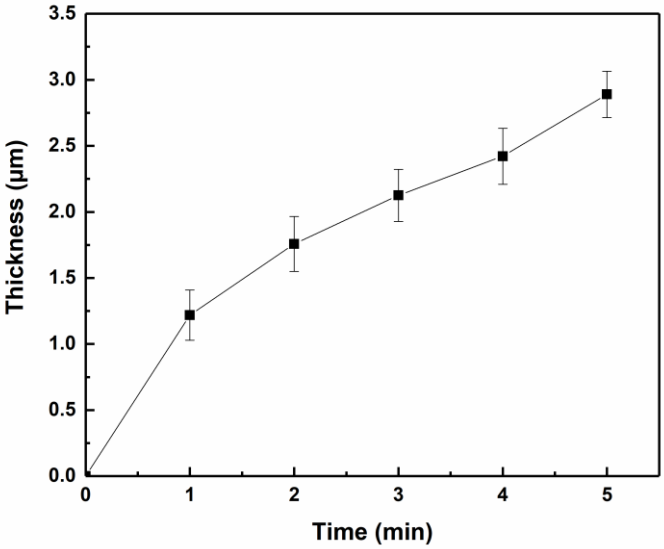

Figure 3.5- Film thickness versus respective electrodeposition time.

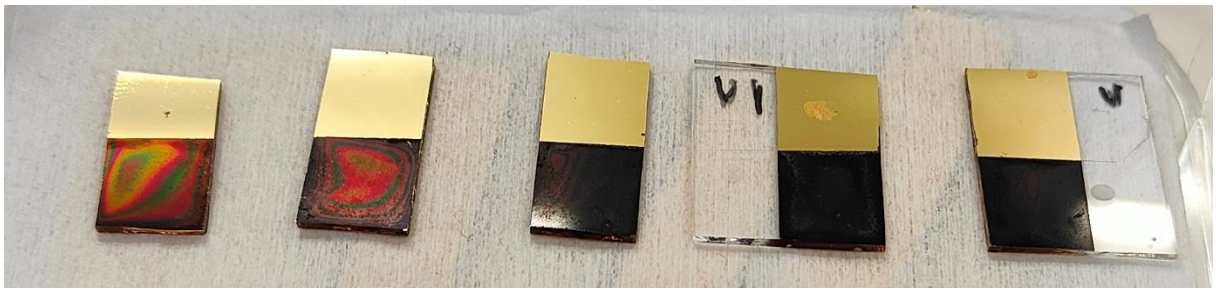

Figure 3.6- Electrodeposited MnO_2 samples obtained at deposition intervals of 60 s, ranging from 1 to 5 min (left to right).

In order to determine the best oxide thickness for improved MSC performance, the samples were characterized through CV. The C_A was calculated for each sample at the 5 mV/s and 30 mV/s scan rates using Equation 1. The measurements were acquired with a 0.5 M K_2SO_4 aqueous electrolyte solution in a three-electrode setup.

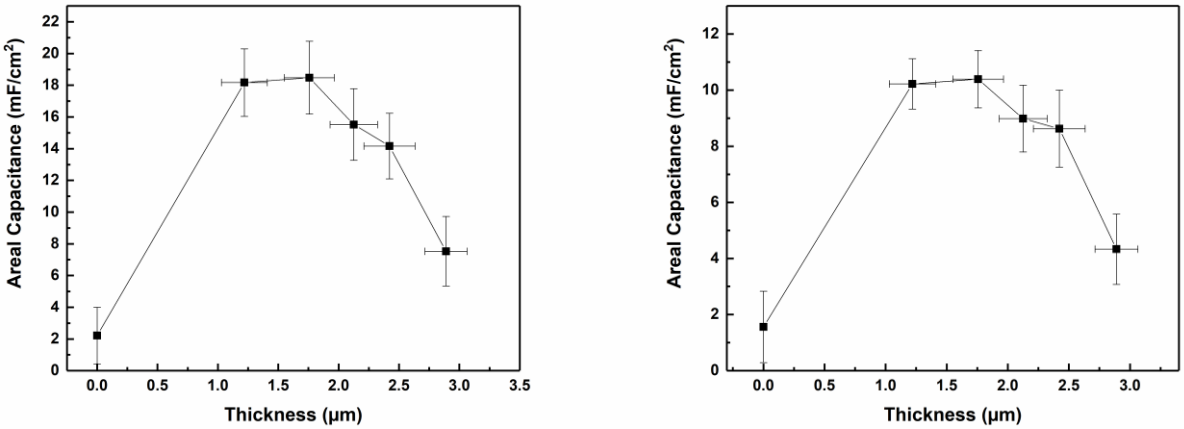

Figure 3.7- Specific areal capacitance versus film thickness, calculated @ 5 mV/s Scan rate (left side); @ 30 mV/s Scan rate (right side).

Table 3- Summary table of obtained electrodeposition data.

Deposition time(min)	Oxide Thickness (μm)	C_A (mF/ cm^2) @ (5 mVs^{-1} Scan rate)
0	--	2.2 ± 1.8
1	1.2 ± 0.2	18 ± 2
2	1.8 ± 0.2	18 ± 2
3	2.1 ± 0.2	16 ± 2
4	2.4 ± 0.2	14 ± 2
5	2.9 ± 0.2	8 ± 2

According to the collected data from Figure 3.7 and Table 3, the best performing oxide thickness was obtained at the 2 minute mark with a 1.8 ± 0.2 μm thickness translating into a 18 ± 2 mF/cm^2 C_A. Although the 1-minute sample presents a similar C_A value, upon visual inspection, the deposition does not achieve homogeneous full coverage of the deposition area, unlike the 2-minute samples. Up until the 2-minute mark, there is an increase in oxide thickness accompanied by an increase in C_A, as seen in the specific capacitance values and in Figure 3.7. However, after the 2-minute mark there is a significant drop in C_A values that persists throughout the remaining time spans (3, 4, and 5 minutes) and respective increasing thicknesses.

According to the literature [26], [27], this phenomenon can be attributed to the poor electrical conductivity of the metal oxides. As the mass loading of MnO_2 increases, so does the ohmic resistance of the electrode. Although the MnO_2 mass loading was not measured throughout the film depositions, if necessary, it could easily be measured by techniques such as quartz crystal microbalance (QCM), surface acoustic wave (SAW) devices, or other mass-sensitive sensors.

The poor electrical conductivity of the metal oxide also makes its specific capacitance highly sensitive to the mass of the active material and the thickness of the electrode. As mass loading increases, it leads to a corresponding increase in electrode thickness, which, in turn, exacerbates ionic mass transfer issues due to restricted ionic conductivity and elevated ohmic resistance (voltage drop) arising from electronic conductivity impairment.

The charge transport kinetics of the ions are influenced by poor electronic conductivity. Simultaneously, it is challenging for the electrolyte to penetrate the electrode film, leading to a reduction in practical specific capacitance.

The solution should represent a trade-off between the performance characteristics of the material in a three-electrode configuration and the energy density and power density achievable in a final device.

3.2.1 Structural and Morphological Characterization of MnO_2

To better understand the composition, structure and morphology of the electrodeposited material, samples were characterized by means of Raman spectroscopy, X-ray Diffraction (XRD), SEM and Optical microscopy (OM).

The Raman spectroscopy, represented in Figure 3.8 (right-side), was carried out on oxide films produced at two distinct settings. The first oxide sample was produced by electrodeposition at -0.65 V for 5 min using a $Mn(CH_3COO)_2$ with Na_2SO_4 solution. The second sample was produced with electro-deposition at -0.95 V for 5 min, using $MnSO_4$ and Na_2SO_4 as precursors. Both oxide samples were produced using the aforementioned parameters and concentrations. After analysing the sample of manganese oxide produced by the electrodeposition of the manganese sulfate solution, the spectrum shows three distinct, well-defined peaks at 993 cm^{-1}, 640 cm^{-1} and 454 cm^{-1}, which can be associated with the presence of MnO_2. The peak at 993 cm^{-1} is typically attributed to the Mn-O bending mode in MnO2, while both the 640 cm^{-1} and 454 cm^{-1} peaks are associated with both Mn-O stretching and bending modes in MnO_2 [28], [29]. For the sample of manganese oxide produced with the manganese acetate solution, the spectrum showed three peaks at 637 cm^{-1}, 553 cm^{-1} and 503 cm^{-1}. According to the literature [28], [29], all these peaks are attributed to the stretching and bending modes of the Mn-O bonds in MnO_2.

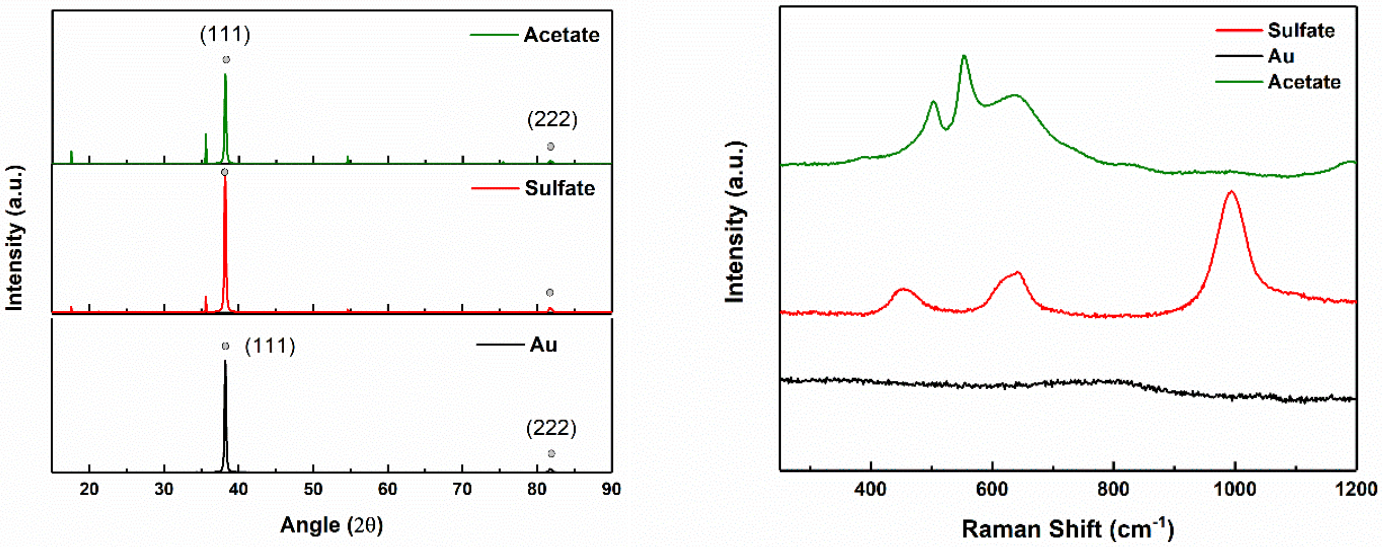

Figure 3.8- X-ray diffractograms (left) and Raman spectra (right) of MnO_2 films produced by $MnSO_4$ (Sulfate) and $Mn(CH_3COO)_2$ (Acetate) precursor solutions.

The obtained XRD diffractograms for both samples, represented in Figure 3.8 (left side), shows two distinct sets of peaks found for both samples. All observed peaks matched for both samples, indicating that despite using different precursors, a similar oxide material was electrodeposited onto the electrodes.

The first set consists of a very intense peak at 38º and a low-intensity peak at 82º, which correspond to the (111) and (222) planes of gold, according to ICDD 00-004-0784 card. The other set consists of a faint peak at around 17.5º, a low-intensity sharp peak at 35.6º and another very faint peak at 54.6º. When analysing the diffractograms against the most common MnO_2 crystalline phases known to be produced through electrodeposition, such as α-MnO_2 (pyrolusite), β-MnO_2 (ramsdellite), and γ-MnO_2 (hollandite), none presented matching peaks. Among these, only α-MnO_2 exhibits characteristic peaks at 18.1º, 36.7º and 56.5º, belonging to the planes (200), (400) and (600) respectively, as reported on JCPDS 00-044-0141. Due to the absence of other characteristic peaks of α-MnO_2 on the diffractograms, its presence in the samples was ruled out, along with the other crystalline phases of MnO_2. Thus, it can be concluded that the electrodeposited manganese oxide is amorphous.

When comparing the unidentified set of peaks against the database similar peak values found in the literature, it was observed that the materials with crystalline phases whose diffractogram peaks most closely matched those of the samples were Ammonium Manganese Chloride (NH_4MnCl_3), Calcium Manganese Oxide ($Ca_{0.8}Mn_8O_{16}$) and Calcium Manganese Oxide Hydrate ($Ca_2Mn_{14}O_{27}$•xH_2O). Upon close inspection of the diffractograms (ICDD 00-050-0015 card; ICDD 00-026-0075 card), only Calcium Manganese Oxide presented matching peaks at 17.5º, 35.6º and 54.5º, belonging to the planes (200), (400) and (600) respectively, as described on JCPDS 00-041-0313. Despite this, other characteristic peaks were not observed in the diffractograms of the samples. Thus, it cannot be said with absolute certainty that it is present in the samples. Assuming that calcium manganese oxide is present in the samples, the calcium ions might have been introduced during electrodeposition

due to reagent impurities, vial contamination or contamination from the glass substrate of the electrodes.

The morphology of the samples was studied by SEM and OM. The MnO_2 sample chosen for SEM and OM analysis was produced from the manganese sulfate solution, as it demonstrated greater suitability for MSC production. The obtained electron micrographs and OM images can be observed in Figure 3.9 and Figure 3.10, respectively.

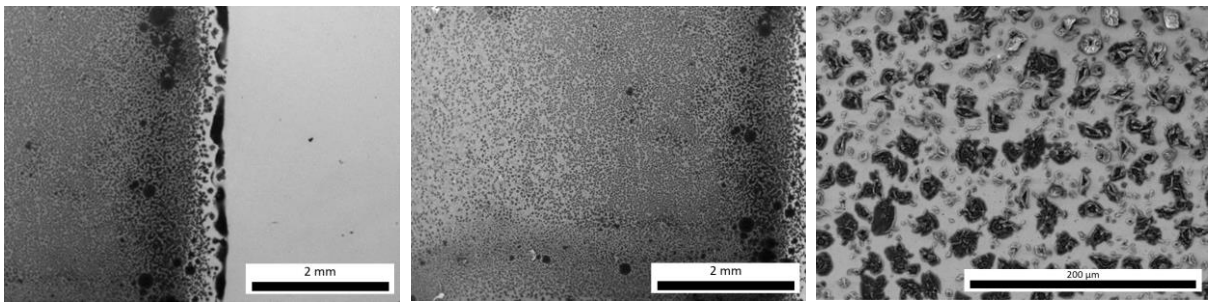

Figure 3.9- SEM images of the MnO_2 film: Border of the electrodeposited region (30x magnification) (left); Central region of the film (30x magnification) (middle); Zoom In on the central region of the film (500x magnification) (right).

When preparing and handling the sample, the oxide layer appeared to be well-defined, uniform, and homogeneous upon visual inspection, as shown in Figure 3.4 (right side). Upon closer examination of the obtained images (Figure 3.9), it becomes clear that the oxide exhibits greater morphological complexity and irregularity than initially perceived.

According to the SEM-EDS mapping (Appendix A.2), there is a nearly homogenous MnO_2 film layer deposited along the gold electrode. This film's presence is also corroborated by the visible color gradient obtained along de deposition area surface, as seen in the optical microscopy images of Figure 3.10. The observed color gradient can be attributed to a variation in film thickness across the surface area. This phenomenon, in conjunction with varying agglomeration densities of oxide particles at distinct zones, induces this optical effect.

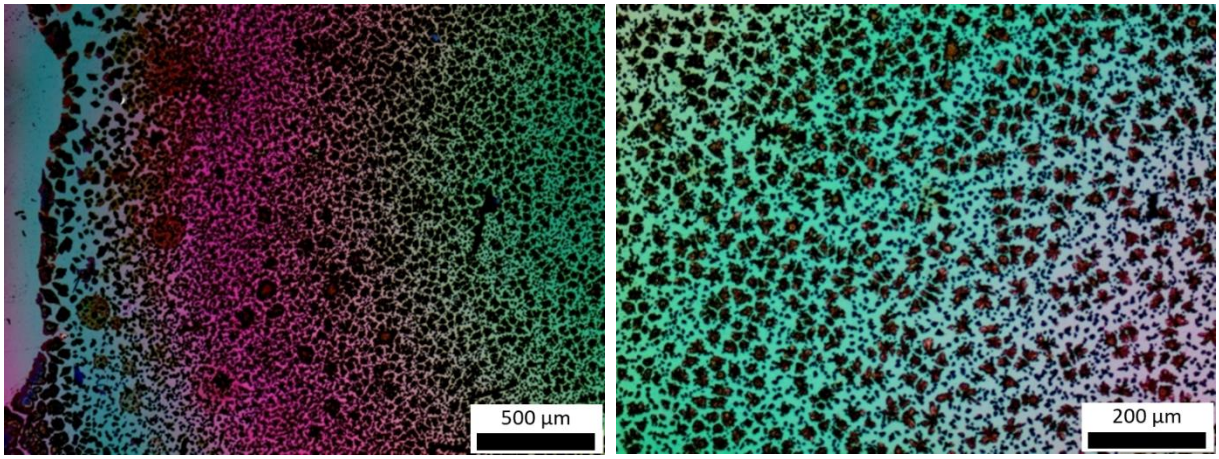

Figure 3.10- Optical microscopy images of the MnO_2 film: Border region of the deposition zone (left); Central region of the film (right).

Particle agglomerates exhibit a pronounced preference for forming at the periphery of the electrode area. Subsequently, their distribution and quantity, while inherently stochastic, exhibit a diminishing trend toward the centre of the electrode. Within the central region, particles and clusters display greater dispersion and smaller size. These MnO_2 particles and clusters overall present irregular shapes and sizes presenting porous nanostructures, this diverse array of nanostructure morphologies can be seen in Appendix A.3.

According to literature [20], the morphology of electrodeposited amorphous MnO_2 preferentially grows horizontally, subsequently forming a compact and layered structure. This morphology is a product of local fluctuations in reactants. With a relatively high deposition potential, the reactant consumption rate is also high, leading to a rapid reaction in the vicinity of the electrode surface. The release of adsorbed water molecules, therefore, leads to the formation of an uneven surface.

3.3 Gel Electrolyte Testing

3.3.1 Electrolyte performance comparison

According to literature [6], [10], [16], both PVA/LiCl and PVA/H_2SO_4 are prime examples of electrolytes commonly used for MSC testing. Being top candidates for adoption in our devices, an electrochemical performance test was done during preliminary testing. This electrochemical characterization was performed for both the PVA/LiCl and PVA/H_2SO_4 electrolytes in Au/Ti electrodes with 600 µm of interdigital spacing, the gel electrolytes were drop casted onto the devices over a fixed area of ~1 cm^2. Measurements were then acquired through the CV and the C_A was calculated using Equation 1 for each electrolyte sample at each measured scan rate.

For both electrolytes, the highest C_A values achieved were calculated for a scan rate of 5 mV/s, namely, 48.7 µF/cm^2 for PVA/LiCl and 33.2 µF/cm^2 for PVA/H_2SO_4. In comparison to PVA/H_2SO_4, the PVA/LiCl gel electrolyte demonstrated higher C_A values across all measured scan rates, as seen in Figure 3.11.

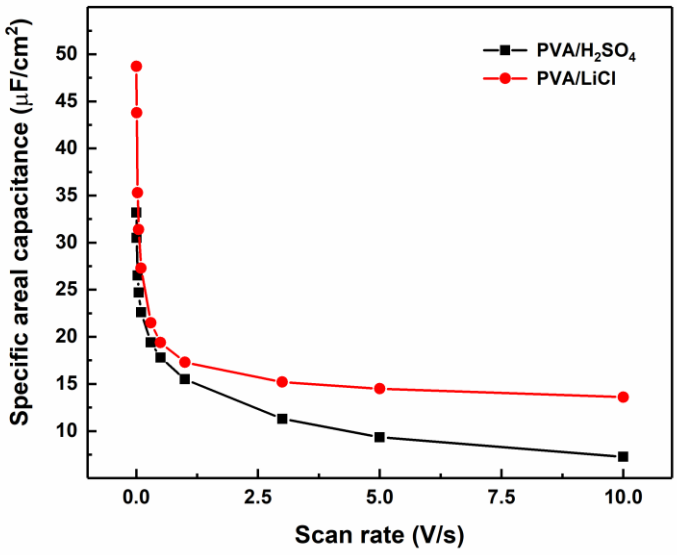

Figure 3.11- Specific capacitance comparison between PVA/LiCl and PVA/H_2SO_4 across all measured scan rates for a 600 µm interdigitated electrode.

Nonetheless, this performance disparity can be attributed to the inherent properties of each respective gel electrolyte according to literature [10]. H_2SO_4 is known to be a strong acid that dissociates completely in water to form hydrogen ions (H^+) and sulfate ions (SO_4^{2-}). Without further dilution, this acid provides a high concentration of hydrogen ions making it a suitable electrolyte for these types of MSC's, since it provides high capacitance. LiCl is a salt that dissociates into lithium ions (Li^+) and chloride ions (Cl^-) in water. LiCl has a lower ionic conductivity compared to H_2SO_4 due to the smaller

size of the Li^+ ion. However, LiCl has a higher specific capacitance than H_2SO_4 due to the high charge density of Li^+ ions and an even higher ionic mobility. This higher mobility, relative to H_2SO_4, allows for faster ion transport and more efficient charge accumulation, resulting in a higher capacitance [10]. These composite gel electrolytes are known to be chemically and thermally stable, as well as resistant to degradation. However, PVA/LiCl also possesses some downsides in comparison with PVA/H_2SO_4. PVA/LiCl is relatively more susceptible to moisture and air, which can reduce its stability. This susceptibility to moisture manifests itself as a change in gel viscosity. With an increase in water content, the ionic mobility of the material increases, thereby indirectly affecting the overall capacitance.

3.3.2 Gel electrolyte compatibility evaluation

In order to ensure compatibility with the nanostructured oxide film, the selected electrolytes underwent preliminary testing to verify their suitability for further MSC development. In total three gel electrolytes were prepared, PVA/H_2SO_4, PVA/H_3PO_4 and PVA/LiCl. The electrolytes were prepared following the previously described protocol and then drop casted onto samples of MnO_2 previously electrodeposited onto Au/Ti electrodes. The oxide for these samples was produced by cathodic electrodeposition at -0.95 V for 2 min using $MnSO_4$ and Na_2SO_4 as precursors at aforementioned parameters and concentrations.

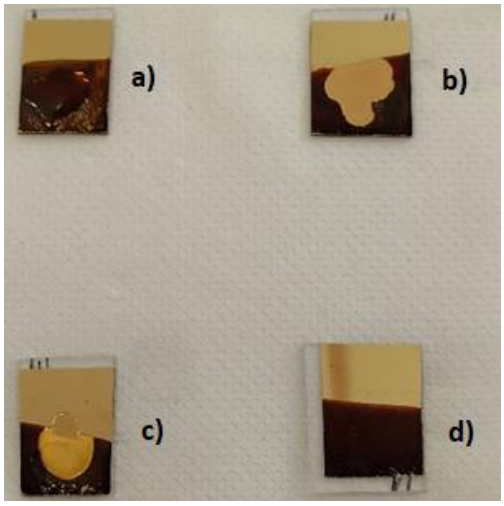

Figure 3.12- Gel electrolytes drop casted onto MnO_2 samples- a) PVA/LiCl; b) PVA/H_2SO_4; c) PVA/H_3PO_4; d) None (control sample).

Upon sample inspection it is observed (as seen in Figure 3.12) that in both b) and c) samples (PVA/H_2SO_4 and PVA/H_3PO_4 respectively) the electrodeposited oxide layer has been dissolved by the composite gel electrolytes. While preparing the gel electrolyte, the medium acidity was not taken into account. Manganese oxides are highly soluble in an acidic medium, with this in mind, further testing with these gel electrolytes was not conducted due to incompatibility with the selected active material. On the other hand, PVA/LiCl (sample a)), revealed to be the most promising option due to its stability and compatibility with other selected materials, thus making it the prime candidate for implementation in our MSC's.

3.4 MSCs: Fabrication and Electrochemical Characterization

After testing and fine tuning each constituent component of the MSC and their respective fabrication process, the next step is to fabricate and fully assemble the device. Based on previous collected data and as stated previously, the chosen electrode configuration for this device is an Au/Ti Interdigital electrode with 600 µm of interdigital spacing. The active material is then electrodeposited on the electrode fingers by using the previously stated optimized conditions. A PVA/LiCl gel electrolyte is then drop casted onto the delimited area.

Upon completing all the steps to manufacture the capacitor (as described in Figure 3.13), the last step was to test its electrochemical performance via cyclic voltammetry (CV). The CV data was obtained within a voltage window of 0.0-0.9 V and at scan rates of 5, 10, 30, 50, 100, 300, 500, 1000, 3000, 5000 and 10000 mV/s.

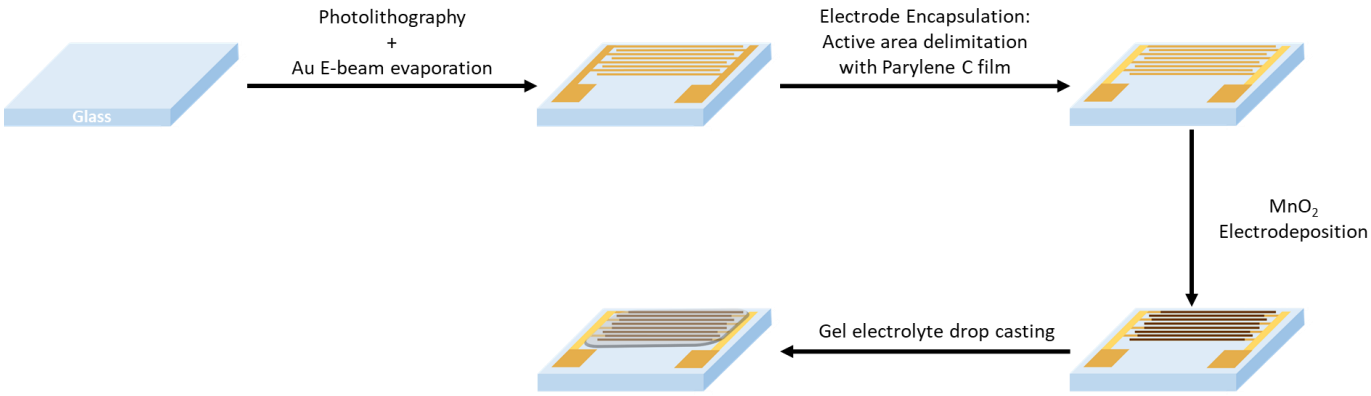

Figure 3.13- Schematic illustration for the fabrication processes of the MSCs. The fabrication procedure includes the following chronological sequencing: Interdigitated electrode production - Photolithography coupled with gold E-beam evaporation - Electrode encapsulation- Parylene-c CVD coupled with lithography - MnO_2 thin film electrodeposition - Gel electrolyte drop casting.

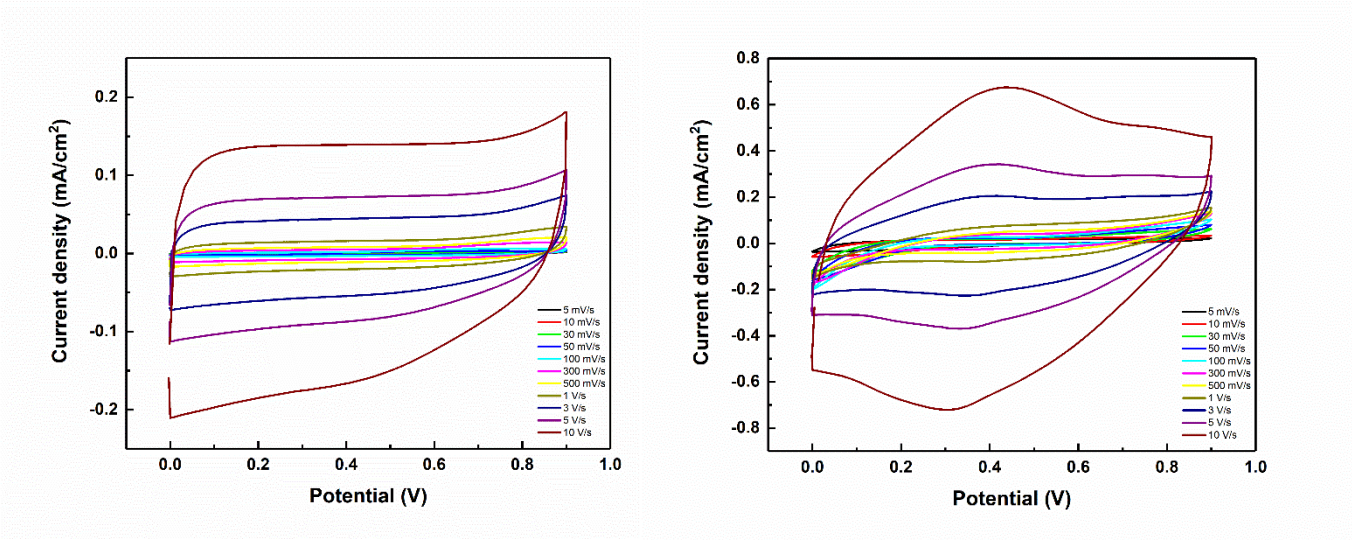

Figure 3.14- CV test on the interdigitated MSC's: without MnO_2 (left) and with MnO_2 (right).

Two distinct MSC's were produced and tested, one with the electrodeposited active material and one without it. The respective CVs, as shown in Figure 3.14, both present rectangular-shaped loops, a characteristic which is the archetypal electric output behaviour of an EDLC.

These CV curves, being sigmoidal in nature, present a sharp rise in current at low potentials that stabilizes for all higher potentials within the voltage window, a behaviour that is clearly observable for all the scan rates above 1 V/s in both devices. Adsorption of ions occurs on the electrode surface as the current increases, along with the increase in potential. The current then stagnates and reaches its maximum value as potential continues to increase, which corresponds to the maximum amount of ions adsorbed on the Au electrode surface. Both CV plots exhibit highly symmetrical curves for the oxidative and reductive scans, indicating excellent electrochemical stability and reaction reversibility.

In the CV of the device without active material (Figure 3.14, left side), a transition from capacitive to resistive behaviour is observed in the anodic and cathodic peaks at the voltage window boundaries. This transition indicates the limit for the working voltage of the device. From the absence of redox peaks on this plot, it is also possible to ascertain that the device is charged and discharged at a constant rate. The observed capacitive behaviour in this device arises from a layer of strongly adsorbed ions on the Au electrode surface, along with a diffuse layer of loosely bound ions and cations.

In Figure 3.14 (right side), the capacitor with MnO_2 exhibits a significantly higher current response than the one without MnO_2 (Figure 3.14, left side). This difference can be attributed to the increased active surface area resulting from the additional layer of material deposited onto the electrodes. This oxide layer, with its porous structure and irregular surface morphology, further enhances the available surface area for surface reactions. However, the dramatic increase in performance is primarily attributed to the way the capacitor now accumulates and stores charge. In addition to displaying EDLC-type behaviour, this capacitor also exhibits clear pseudocapacitive behaviour, as evidenced by the observable redox peaks seen in the oxidative and reductive scans shown in Figure 3.14 (right side). This

information confirms that the capacitor with MnO_2 likely stores energy through a combination of pseudocapacitance from MnO_2 and double-layer capacitance from the Au interdigital electrodes.

According to literature, manganese oxide is often categorized as a pseudocapacitive material within the realm of electrochemical energy storage devices. This pseudocapacitance originates from reversible faradaic redox reactions occurring at the electrode surface. These reactions involve the exchange of electrons between the electrode surface material and the ion species present in the electrolyte. The quasi-symmetrical redox peaks seen in Figure 3.14 (right side) may imply the presence of some redox couples with different formal potentials. These sharp peaks in the plot may reflect the completion of the onset redox reaction. In literature [30] it has been documented that MnO_2 exhibits multiple redox couples, with MnO_2/Mn_2O_3 and Mn_2O_3/MnO being two of the most observed pairs. To fully identify the oxidation state of the present species, XPS could be employed for a more in-depth analysis.

Using Equation 2 and the CV data, the current density was calculated for each specific capaci-tance, the respective plots for each MSC were then created, as shown in Figure 3.15.

$$I = C\,\frac{dV}{dt} \tag{2}$$

Where I Is the measured current, C is the specific capacitance calculated from the cyclic voltammograms and dV/dt Is the measurement's scan rate.

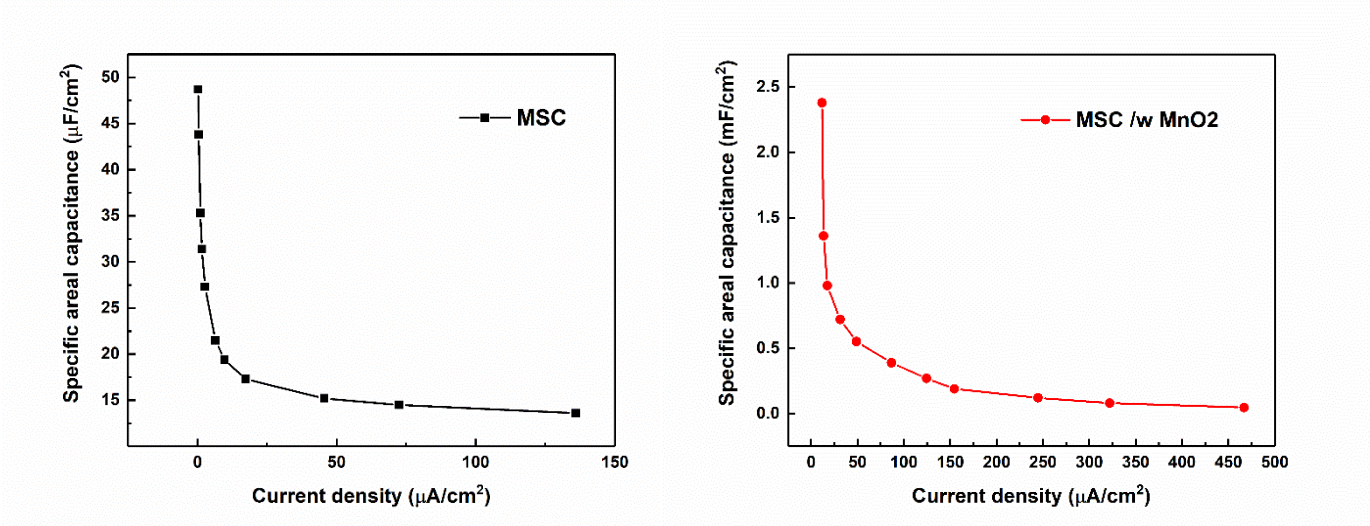

Figure 3.15- Specific capacitance by current density test on the interdigitated MSC without MnO_2 (left plot) and with MnO_2 (right plot).

As shown in Figure 3.15, an inverse correlation is evident between current density and specific areal capacitance. To be more precise, when current density rises, the specific capacitance decreases.

As seen in Figure 3.15 (left plot), the MSC without MnO_2 displayed a relatively lower specific areal capacitance of 48.70 $\mu F/cm^2$ at a current density of 0.24 $\mu A/cm^2$. By comparing both plots, Figure 3.15 (left and right), it can be observed that both are exhibiting steep drops in capacitance as current increases. This behaviour suggests that both MSCs possess a limited operating range for energy storing purposes and using it outside of that range will likely result in diminished performance. The MSC with MnO_2, represented in Figure 3.15 (right plot), exhibited a specific areal capacitance of 2.38 mF/cm^2 at a current density of 11.9 $\mu A/cm^2$. Considering the same scan rates for each device, there was a significant increase in both specific capacitance and current densities with the addition of MnO_2, as expected. However, at a slightly higher current density of 13.6 $\mu A/cm^2$, the specific areal capacitance decreased to 1.36 mF/cm^2, nearly halving the effective capacitance value. This indicates a significant drawback in device effectiveness and capacitance value retention as current increases. For a more comprehensive analysis, coulombic efficiency should be tested through galvanostatic charge/discharge (GCD).

3.4.1 Assembly and Characterization of Flexible MSCs

In order to test our MSC implementation on a flexible substrate, another set of devices were produced by adding a step in the fabrication procedure. The added step consisted in depositing a thin layer (11.5 ± 1.5 μm) of parylene-C on a supporting glass substrate [31]. Parylene-C stands out as a versatile material with commendable mechanical properties, flexibility, biostability, and biocompatibility, making it an optimal substrate for applications in wearable technology, medical devices, and on-skin devices. Its favorable attributes include the ability to produce ultrathin and conformable membranes. Notably, parylene-C seamlessly aligns with standard microelectronics processing techniques while maintaining its biofriendly characteristics, further highlighting its adaptability and utility in various applications [31].

The Au/Ti electrodes were subsequently deposited and patterned onto the parylene substrate, with the chosen electrode configuration being the interdigital electrode with a 600 μm of interdigital spacing.

Post encapsulation, the manganese oxide was then electrodeposited onto the delimited interdigital section of the electrode. Upon visual inspection, the MnO_2 film appears to retain its properties, with the adhesion remaining unaffected by the change in process. Even though the MnO_2 film is inherently brittle, the flexing of the substrate doesn't cause any tears or fractures along the MnO_2 film's surface.

Upon completion of the electrodeposition process, the parylene layer was then peeled off from the supporting glass substrate by partially cutting the edge of the substrate's non patterned area with a scalpel and heating the samples in water at 90 ºC until the thin parylene layer is lifted and detached from the glass, a methodology adapted from R. Correia et al. [31]. This process was conducted before the electrolyte was deposited to prevent the dissolution of the electrolyte in the heated water. The samples are then dried at room temperature and the gel electrolyte is finally applied to the MSCs. The final product can be seen in Figure 3.16.

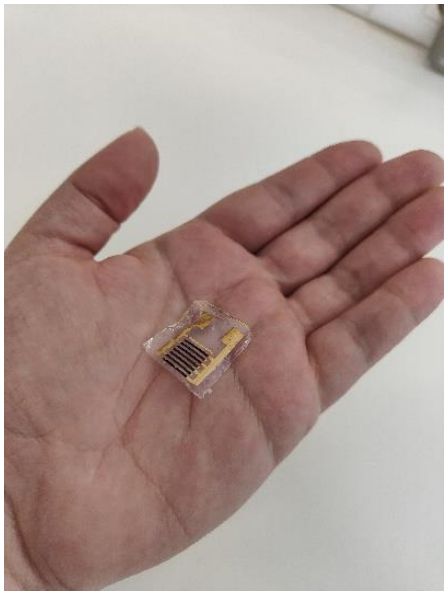

Figure 3.16- Flexible Interdigitated MSC with optimized MnO_2 thin film.

After completing all the manufacturing steps, the last step involved testing its electrochemical performance via cyclic voltammetry (CV). The electrochemical properties were not tested in conjunction with bending tests. The CV data was once again obtained within a voltage window of 0.0-0.9 V and at scan rates of 5, 10, 30, 50, 100, 300, 500, 1000, 3000, 5000 and 10000 mV/s.

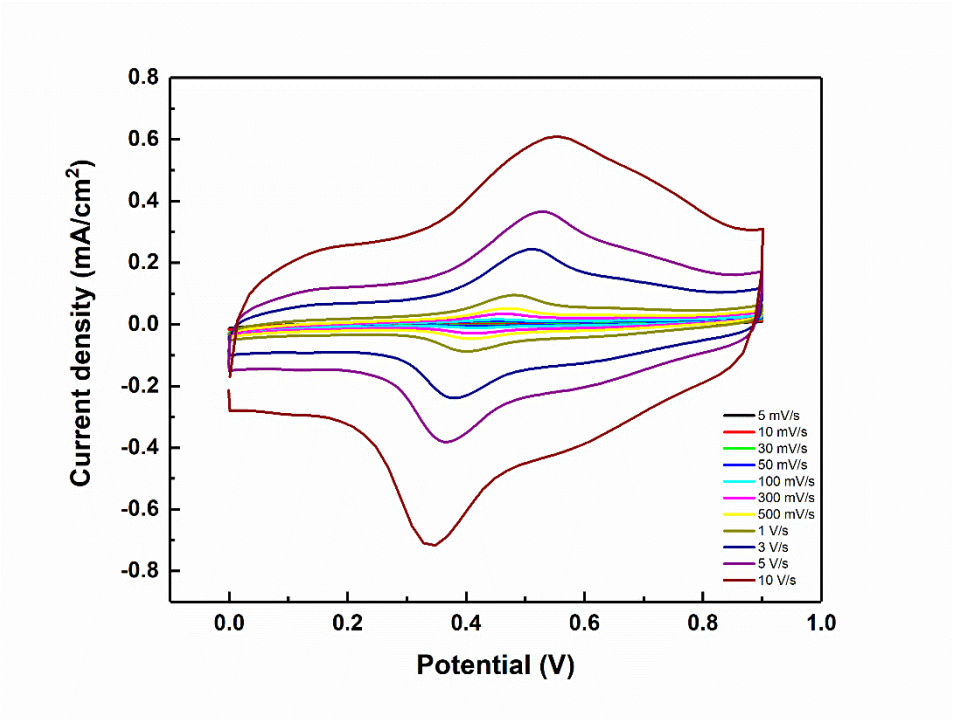

Figure 3.17- CV test on the flexible interdigitated MSC with MnO_2.

As seen in previous devices, the cyclic voltammogram of the flexible MSC (Figure 3.17), exhibits a sigmoidal curve for scan rates above 500 mV/s. This curve features a sharp increase in current at low potentials, followed by stabilization, which persists across all higher potentials within the voltage window. The plot displays symmetrically shaped curves with prominent redox peaks. The symmetric curves indicate good electrochemical stability and reversibility. However, the redox peaks appear to be slightly mismatched within a voltage window of 0.2 V. The device clearly exhibits both pseudocapaci-tance and EDLC-type behaviour. The sharp redox peaks observed in the plot suggest, once again, the presence of redox couples. According to the literature, MnO_2/Mn_2O_3 and Mn_2O_3/MnO are the most likely observed pairs.

As before, with the data gathered from the CV, the specific areal capacitance was calculated using Equation 1. This flexible iteration of the MSCs exhibited a specific areal capacitance of 0.59 ± 0.084 mF/cm^2 (at a current density of 2.93 μA/cm^2).

3.4.2 Flexible MSC Performance Analysis and Comparison

After fabricating the devices and conducting electrochemical testing, further examination of the gathered data was conducted. As mentioned previously, the device with MnO_2 exhibits significantly higher currents at each potential value than the device without MnO_2. This current response is observed for all measured scan rates, as seen by comparing the cyclic voltammograms of Figure 3.14.

In Figure 3.18, by comparing the currents side by side for the same scan rate (5 mV/s), the disparity in currents for each device can be clearly seen. By taking the integrated absolute area of the cyclic voltammogram plots, we can calculate the specific areal capacitance of each device for all measured scan rates using Equation 1. The MSC with MnO_2 presents a CV plot with a much larger absolute area than the plot of the MSC without it. Thus, with Equation 1, it translates into a relatively higher specific capacitance value for all the slower scan rates, as shown in Figure 3.19.

The difference in capacitance value for the MSC with and without MnO_2 seen in Table 4 and Figure 3.19 is to be expected. It is known that the pseudocapacitance contribution brought in by the oxide is 10 to 100 times larger than only the double-layer capacitance. This effect, coupled with the tuning of the active surface material's morphology and thickness, contributes to a highly expressive specific capacitance value.

One of the most important parameters to calculate and compare for each device is the energy density. For the calculation of the energy density (E_D), the following equation was used:

$$E_D = \frac{1}{2} \times C_A \times (\Delta V)^2 \quad (3)$$

$\boldsymbol{C_A}$ being the specific areal capacitance and $\Delta \boldsymbol{V}$ the voltage window.

As seen in Table 4, the device that possesses the higher energy density is the MSC with MnO_2 (0.27 µWh/cm^2), followed by the flexible MSC with MnO_2 (66.4 nWh/cm^2). The bare electrodes, as expected, display a much lower value (5.48 nWh/cm^2).

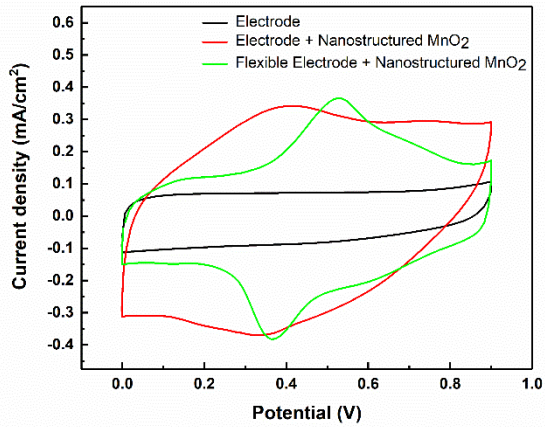

Figure 3.18- CV scan comparison for the produced MSC variants, displayed at a singular Scan rate of 5 V/s.

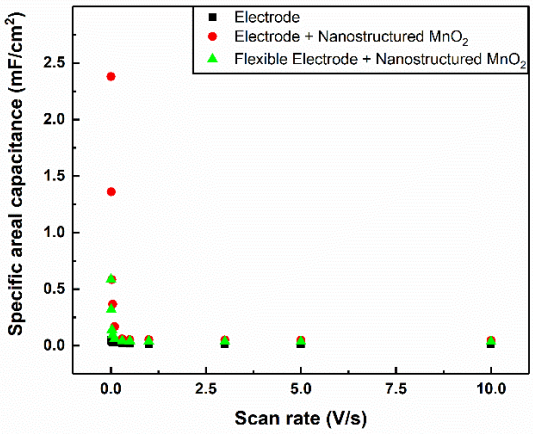

Figure 3.19- Specific capacitance comparison between MSC variants across all measured scan rates.

In theory, the flexible MSC with MnO_2 should not deviate much in terms of capacitance value from its non-flexible counterpart. However, the produced devices exhibited a slight deviation in capacitance value relative to the non-flexible devices, presenting a lower capacitance than expected for all measured scan rates. By comparing Figure 3.14 (right side) against Figure 3.17, we can observe that the flexible MSC displays lower currents for all scan rates compared to its non-flexible counterpart, a behaviour that is clearly seen for the scan rate of 5 V/s in Figure 3.18. However, for redox peaks at scan rates faster than 300 mV/s and slower than 10 V/s, it is noted that the flexible MSC exhibits redox peaks with a higher peak current than that of the non-flexible MSC. The peak current values are only similar for both devices at the last measured scan rate of 10 V/s.

The disparity in the overall specific capacitance values for flexible MSCs and non-flexible MSCs, as seen in Table 4, can be attributed to factors such as fabrication process variability and gel electrolyte water content fluctuation.

In any fabrication process, there is always some level of inherent process variability. Due to the experimental nature of our process, we were only able to produce a limited number of samples, which allows us to identify outliers and visually non-conforming samples.

During the last step of the MSC assembly the gel electrolytes were applied and left to dry overnight. However, this approach did not involve any ambient humidity control, which turned out to be problematic. Humidity, as an uncontrolled variable, might pose a potential problem for the device's stability. The water content naturally might fluctuate over time, potentially leading to issues such as the fluidification of the gel or, on the other hand, an increase in viscosity due to a decrease in water content. These variations in water content, directly impact the gel electrolyte's ionic mobility. Consequently, the change in ionic mobility indirectly affects the capacitance of the MSC.

Table 4- Summary table of obtained MSC specific capacitance and energy density.

	Electrode	Electrode + Nanostructured MnO_2	Flexible Electrode + Nanostructured MnO_2
C_A @ (5 mVs^{-1} Scan rate)	48.70 ±0.04 $\mu F/cm^2$	2.38 ± 0.62 mF/cm^2	0.59 ± 0.084 mF/cm^2
Energy density	5.48 nWh/cm^2	0.27 $\mu Wh/cm^2$	66.4 nWh/cm^2

4

CONCLUSIONS AND FUTURE PROSPECTS

Through a photolithographic process, several configurations of interdigital planar electrodes were successfully produced. Through electrochemical characterization, it was proved that, for the electrode designs employed, the interdigital spacing of the electrodes did not significantly affect device performance.

To evaluate and fine-tune the electrodeposition process, several MnO_2 films were produced using distinct precursor solutions and applied deposition potentials. A solution consisting of $MnSO_4$ (0.15 M) and Na_2SO_4 (0.1 M), with an electrodeposition potential of -0.95 V, was found to be the optimal setting for MnO_2 film growth. The optimal deposition time, which yields the highest measured capacitance, was found to be 2 minutes, resulting in a film thickness of 1.76 ± 0.21 μm and a corresponding specific capacitance of 18.48 ± 2.29 mF/cm². A correlation was found between deposition time and film thickness. After the first minute of deposition, the growth of the oxide layer thickness is linear with a slope of 0.4 μm/min.

Sample characterization through Raman spectroscopy and XRD, confirmed that the grown layer was composed of amorphous MnO_2. XRD analysis suggests that there might exist $Ca_{0.8}Mn_8O_{16}$ polycrystalline aggregates, thus suggesting an unidentified source of calcium ions during the electrodeposition process. In accordance with the SEM-EDS mapping and Optical microscopy imagery, a nearly homogeneous MnO_2 film layer is evident along the gold electrode. However, there is observable variation in film thickness across the surface area. Additionally, there are oxide clusters that exhibit irregular shapes and sizes, thereby forming porous nanostructures with a diverse array of morphologies.

For the final iteration of produced MSCs, both PVA/LiCl and PVA/H_2SO_4 composite gel electrolytes were tested through electrochemical characterization. The PVA/LiCl gel electrolyte exhibited better overall performance and a higher specific capacitance. To ensure compatibility with the chosen active material, PVA/H_2SO_4, PVA/H_3PO_4 and PVA/LiCl gel electrolytes were tested. Due to their medium acidity, acidic electrolytes such as PVA/H_2SO_4 and PVA/H_3PO_4 dissolved the oxide layers. Therefore, PVA/LiCl stands as the sole practical choice among the considered electrolytes.

After fine-tuning the constituent components of the interdigitated MSC, its final iteration was constructed. The obtained results shown that the interdigitated MSCs exhibited a capacitance of 48.70 ± 0.04 μF/cm^2 (0.24 μA/cm^2) without MnO_2 and 2.38 ± 0.62 mF/cm^2 (11.9 μA/cm^2) with MnO_2, respectively. Thereby displaying a significant increase in both capacitance and current densities with the addition of the nanostructured MnO_2 layer.

In an effort to create flexible MSCs, the fabrication process was adapted to accommodate a flexible substrate, specifically a parylene-C film. Subsequently, a flexible interdigitated MSC with MnO_2 was successfully manufactured, demonstrating a capacitance of 0.59 ± 0.084 mF/cm^2 (2.93 μA/cm^2).

The results we obtained align with the findings of Zhang et al. [16], with values falling within the same order of magnitude (3.29 mF/cm^2 areal capacitance at a current density of 5.6 μA/cm²). However, we were able to improve upon and achieve comparable areal capacitance values using thin films with minimal MnO_2 loadings. In contrast, the studies referenced here report high MnO_2 mass loadings, resulting in thicker films.

Further research could explore methods for optimizing the interdigitated electrode design while also considering surface texture enhancements. This approach aims to expand the active area and increase capacitance, consequently enhancing the energy density of capacitors. For this purpose, strategies such as designing electrodes with different interdigital spacing configurations, selectively eroding the substrate into which the electrodes are patterned, or even eroding the electrode's surface itself, can be an interesting approach.

Regarding the active material, in principle, according to the literature, MnO_2 produced through a precursor solution of manganese acetate ($Mn(CH_3COO)_2$) should be somewhat equivalent to manganese sulfate ($MnSO_4$) in terms of adhesion to a gold substrate, mechanical behaviour, and homogeneity of deposition. However, in our experimental settings, this was not the case. The produced oxide layer had an extremely high tendency to crumble and fall from the electrode, leading to a loss of material and thus presenting very low adhesion to the gold substrate. A further investigation into the reasons behind this phenomenon is warranted.

By employing thin nanostructured MnO_2 layers to texturize the MSC's interdigitated electrode surface, ultra-high capacitances and current densities cannot be achieved. To achieve this, a substantial increase in the specific mass loading of MnO_2 in the electrodes would be required.

However, this was not the approach we wanted to take, nor was it aligned with the main objectives of the thesis.

Conversely, an opposite approach could be taken with the goal of further texturizing the electrode's surface and increasing performance. By substantially increasing the specific loading mass of MnO_2 in the electrodes, we could begin to grow nanorods through electrodeposition, according to the literature. This would introduce a degree of intercalation pseudocapacitance to the MSC and can effectively narrow the gap between supercapacitors and lithium-ion batteries in energy density and power density.

To further enhance performance, another approach could be considered, increasing the mass loadings of the geometric surface area. Traditionally, scientists apply a thin coating of electroactive substances to highly porous three-dimensional (3-D) substrates. These substrates often consist of materials like nickel foams or carbon structures, which typically have a thickness ranging from several microns to millimeters. This approach brings the active material loadings into the range used in commercial standards.

Furthermore, in order to enhance the final iteration of the produced MSCs, we can implement improvements to further optimize their functionality. One key improvement is to encapsulate the active area containing the gel electrolyte to prevent electrolyte leakage and maintain a constant water content

in the PVA gel matrix. The performance of the MSCs could be studied by varying electrolyte concentrations and exploring alternative non-acidic gel electrolytes. This approach would help us gain a better understanding of how ion size and concentration affect the electrochemical performance of the device. Non-aqueous electrolytes, such as ionic liquids, could also be a viable alternative for MSCs, thus avoiding the inherent limitations of using water-based systems.

To comprehensively analyse the final iterations of the produced MSC's performance, additional tests would be necessary. This would entail conducting a broader range of characterization tests, includ-ing XPS (X-ray Photoelectron Spectroscopy), galvanostatic charge/discharge (GCD), EIS (Electro-chemical Impedance Spectroscopy), cyclability tests, sheet resistance measurement, power density ver-sus energy density analysis, and finally, performing bending tests to evaluate the mechanical properties of the device for potential application in flexible technologies.

In conclusion, we have successfully conducted a comprehensive evaluation and tuning of a methodology for nanostructuring interdigital planar microsupercapacitor (MSC) electrodes through the electrodeposition of thin MnO_2 nanostructured films. We also successfully demonstrated the versatility of this approach by texturizing flexible planar interdigitated electrodes.

BIBLIOGRAPHY

[1] J. Li *et al.*, "Calligraphy-inspired brush written foldable supercapacitors," *Nano Energy*, vol. 38, pp. 428–437, Aug. 2017, doi: 10.1016/j.nanoen.2017.06.013.

[2] Y. Ko, M. Kwon, W. K. Bae, B. Lee, S. W. Lee, and J. Cho, "Flexible supercapacitor electrodes based on real metal-like cellulose papers/639/4077/4079/4105/639/301/299/1013 article," *Nat Commun*, vol. 8, no. 1, Dec. 2017, doi: 10.1038/s41467-017-00550-3.

[3] R. Jia, G. Shen, F. Qu, and D. Chen, "Flexible on-chip micro-supercapacitors: Efficient power units for wearable electronics," *Energy Storage Mater*, vol. 27, pp. 169–186, May 2020, doi: 10.1016/j.ensm.2020.01.030.

[4] F. Li *et al.*, "Stamping Fabrication of Flexible Planar Micro-Supercapacitors Using Porous Graphene Inks," *Advanced Science*, vol. 7, no. 19, Oct. 2020, doi: 10.1002/advs.202001561.

[5] A. Velasco *et al.*, "Recent trends in graphene supercapacitors: From large area to micro-supercapacitors," *Sustainable Energy and Fuels*, vol. 5, no. 5. Royal Society of Chemistry, pp. 1235–1254, Mar. 07, 2021. doi: 10.1039/d0se01849j.

[6] J. Coelho, M. P. Kremer, S. Pinilla, and V. Nicolosi, "An outlook on printed microsupercapacitors: Technology status, remaining challenges, and opportunities," *Current Opinion in Electrochemistry*, vol. 21. Elsevier B.V., pp. 69–75, Jun. 01, 2020. doi: 10.1016/j.coelec.2019.12.004.

[7] M. Lu, *Supercapacitors: materials, systems, and applications*. John Wiley & Sons, 2013.

[8] Q. Meng, K. Cai, Y. Chen, and L. Chen, "Research progress on conducting polymer based supercapacitor electrode materials," *Nano Energy*, vol. 36. Elsevier Ltd, pp. 268–285, Jun. 01, 2017. doi: 10.1016/j.nanoen.2017.04.040.

[9] Y. Jiang and J. Liu, "Definitions of Pseudocapacitive Materials: A Brief Review," *Energy and Environmental Materials*, vol. 2, no. 1. John Wiley and Sons Inc, pp. 30–37, Mar. 01, 2019. doi: 10.1002/eem2.12028.

[10] C. Zhong, Y. Deng, W. Hu, J. Qiao, L. Zhang, and J. Zhang, "A review of electrolyte materials and compositions for electrochemical supercapacitors," *Chemical Society Reviews*, vol. 44, no. 21. Royal Society of Chemistry, pp. 7484–7539, Nov. 07, 2015. doi: 10.1039/c5cs00303b.

[11] C. (John) Zhang *et al.*, "Additive-free MXene inks and direct printing of micro-supercapacitors," *Nat Commun*, vol. 10, no. 1, Dec. 2019, doi: 10.1038/s41467-019-09398-1.

[12] J. Sun *et al.*, "Printable nanomaterials for the fabrication of high-performance supercapacitors," *Nanomaterials*, vol. 8, no. 7. MDPI AG, Jul. 13, 2018. doi: 10.3390/nano8070528.

[13] Q. Xue *et al.*, "Recent Progress on Flexible and Wearable Supercapacitors," *Small*, vol. 13, no. 45, Dec. 2017, doi: 10.1002/smll.201701827.

[14] N. Liu and Y. Gao, "Recent Progress in Micro-Supercapacitors with In-Plane Interdigital Electrode Architecture," *Small*, vol. 13, no. 45, Dec. 2017, doi: 10.1002/smll.201701989.

[15] J. Zhang, G. Zhang, T. Zhou, and S. Sun, "Recent Developments of Planar Micro-Supercapacitors: Fabrication, Properties, and Applications," *Advanced Functional Materials*, vol. 30, no. 19. Wiley-VCH Verlag, May 01, 2020. doi: 10.1002/adfm.201910000.

[16] C. Zhang, J. Xiao, L. Qian, S. Yuan, S. Wang, and P. Lei, "Planar integration of flexible micro-supercapacitors with ultrafast charge and discharge based on interdigital nanoporous gold electrodes on a chip," *J Mater Chem A Mater*, vol. 4, no. 24, pp. 9502–9510, 2016, doi: 10.1039/c6ta02219g.

[17] N. Liu and Y. Gao, "Recent Progress in Micro-Supercapacitors with In-Plane Interdigital Electrode Architecture," *Small*, vol. 13, no. 45, Dec. 2017, doi: 10.1002/smll.201701989.

[18] S. Zheng, X. Shi, P. Das, Z. S. Wu, and X. Bao, "The Road Towards Planar Microbatteries and Micro-Supercapacitors: From 2D to 3D Device Geometries," *Advanced Materials*, vol. 31, no. 50, Dec. 2019, doi: 10.1002/adma.201900583.

[19] D. Wu *et al.*, "MnO2/Carbon Composites for Supercapacitor: Synthesis and Electrochemical Performance," *Frontiers in Materials*, vol. 7. Frontiers Media S.A., Feb. 11, 2020. doi: 10.3389/fmats.2020.00002.

[20] C. P. Yi and S. R. Majid, "The Electrochemical Performance of Deposited Manganese Oxide-Based Film as Electrode Material for Electrochemical Capacitor Application," in *Semiconductors - Growth and Characterization*, InTech, 2018. doi: 10.5772/intechopen.71957.

[21] N. Wang, J. Liu, Y. Zhao, M. Hu, and G. Shan, "High-performance asymmetric micro-supercapacitors based on electrodeposited MnO2 and N-doped graphene," *Nanotechnology*, vol. 30, no. 23, Mar. 2019, doi: 10.1088/1361-6528/ab0bd8.

[22] J. Han *et al.*, "On-Chip Micro-Pseudocapacitors for Ultrahigh Energy and Power Delivery," *Advanced Science*, vol. 2, no. 5, May 2015, doi: 10.1002/advs.201500067.

[23] L. Y. Chen *et al.*, "High-energy-density nonaqueous MnO2@nanoporous gold based supercapacitors," *J Mater Chem A Mater*, vol. 1, no. 32, pp. 9202–9207, Aug. 2013, doi: 10.1039/c3ta11480e.

[24] X. Wang, B. D. Myers, J. Yan, G. Shekhawat, V. Dravid, and P. S. Lee, "Manganese oxide micro-supercapacitors with ultra-high areal capacitance," *Nanoscale*, vol. 5, no. 10, pp. 4119–4122, May 2013, doi: 10.1039/c3nr00210a.

[25] T. S. Mathis, N. Kurra, X. Wang, D. Pinto, P. Simon, and Y. Gogotsi, "Energy Storage Data Reporting in Perspective—Guidelines for Interpreting the Performance of Electrochemical Energy Storage Systems," *Advanced Energy Materials*, vol. 9, no. 39. Wiley-VCH Verlag, Oct. 01, 2019. doi: 10.1002/aenm.201902007.

[26] H. Wang *et al.*, "Graphene-nickel cobaltite nanocomposite asymmetrical supercapacitor with commercial level mass loading," *Nano Res*, vol. 5, no. 9, pp. 605–617, 2012, doi: 10.1007/s12274-012-0246-x.

[27] J. Yang, L. Lian, H. Ruan, F. Xie, and M. Wei, "Nanostructured porous MnO2 on Ni foam substrate with a high mass loading via a CV electrodeposition route for supercapacitor application," *Electrochim Acta*, vol. 136, pp. 189–194, Aug. 2014, doi: 10.1016/j.electacta.2014.05.074.

[28] J. E. Post, D. A. McKeown, and P. J. Heaney, "Raman spectroscopy study of manganese oxides: Tunnel structures," *American Mineralogist*, vol. 105, no. 8, pp. 1175–1190, Aug. 2020, doi: 10.2138/am-2020-7390.

[29] A. Ogata, S. Komaba, R. Baddour-Hadjean, J. P. Pereira-Ramos, and N. Kumagai, "Doping effects on structure and electrode performance of K-birnessite-type manganese dioxides for rechargeable lithium battery," *Electrochim Acta*, vol. 53, no. 7, pp. 3084–3093, Feb. 2008, doi: 10.1016/j.electacta.2007.11.038.

[30] C. Lucas *et al.*, "Preparation and characterization of Ca 1∈-∈x Ce x MnO 3 perovskite electrodes," *Journal of Solid State Electrochemistry*, vol. 13, no. 6, pp. 943–950, Jun. 2009, doi: 10.1007/s10008-008-0630-3.

[31] R. Correia *et al.*, "Biocompatible Parylene-C Laser-Induced Graphene Electrodes for Microsupercapacitor Applications," *ACS Appl Mater Interfaces*, vol. 14, no. 41, pp. 46427–46438, Oct. 2022, doi: 10.1021/acsami.2c09667.

A

APPENDIXES

A.1 Cyclic Voltammograms of each Electrode Designs

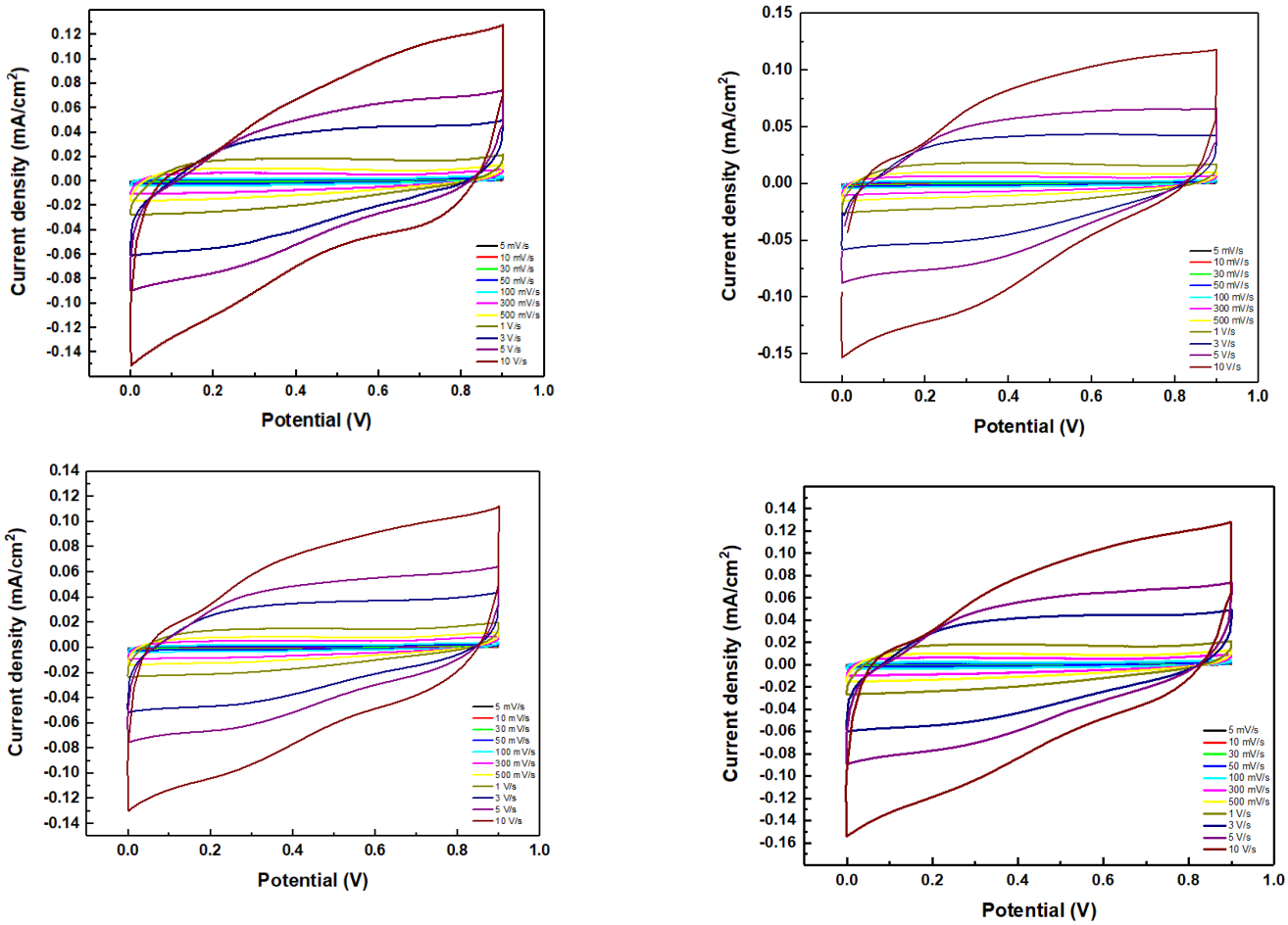

Appendix A.1.1- CVs of interspaced electrodes designs:
100 µm (top-left); 200 µm (top-right); 400 µm (bottom left) and 600 µm (bottom right).

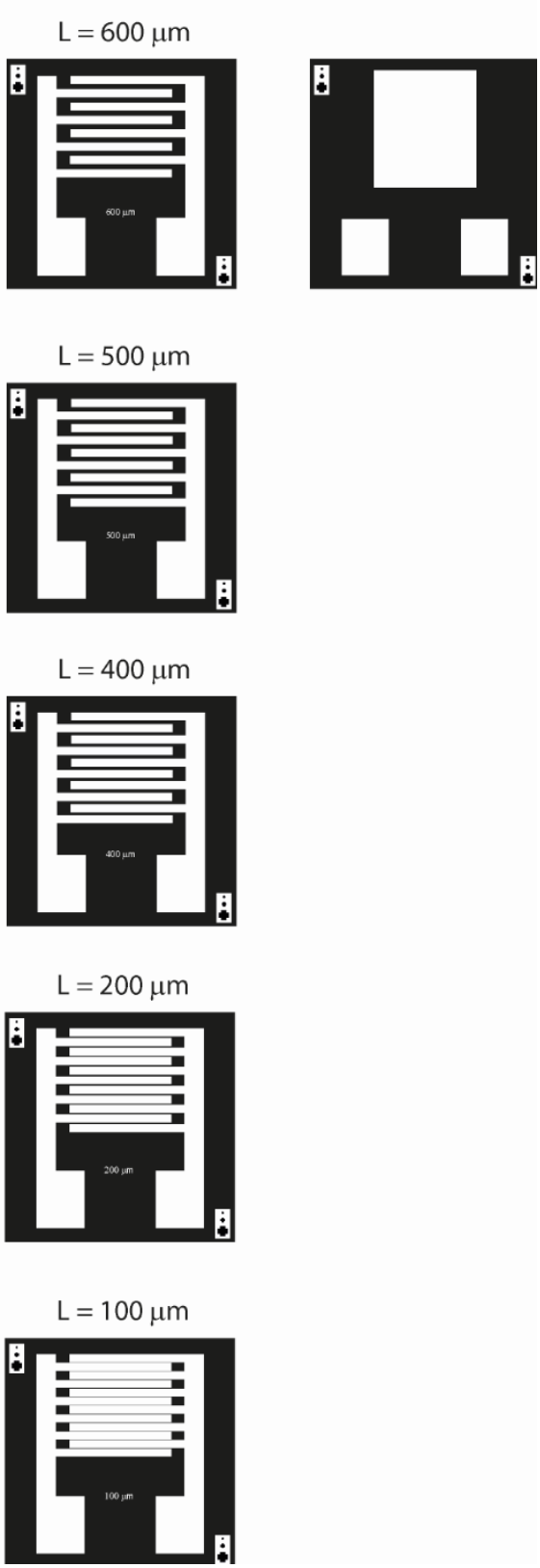

Appendix A.1.2- Interspaced electrode designs (L=interspacing distance).

A.2 SEM-EDS Mapping

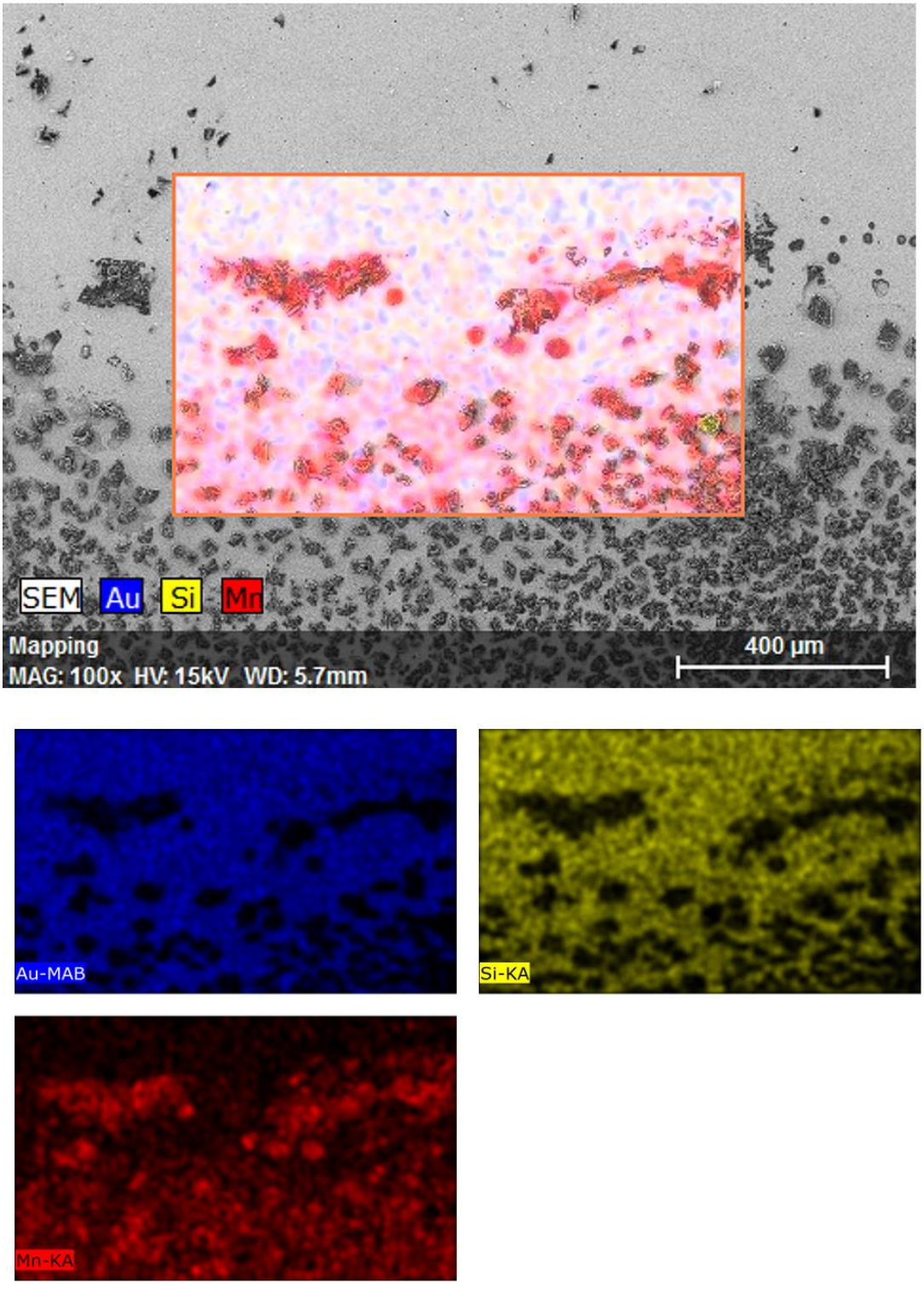

Appendix A.2- SEM-EDS Mapping.

A.3 Microscopy Imagery of MnO2 Films and Nanostructures

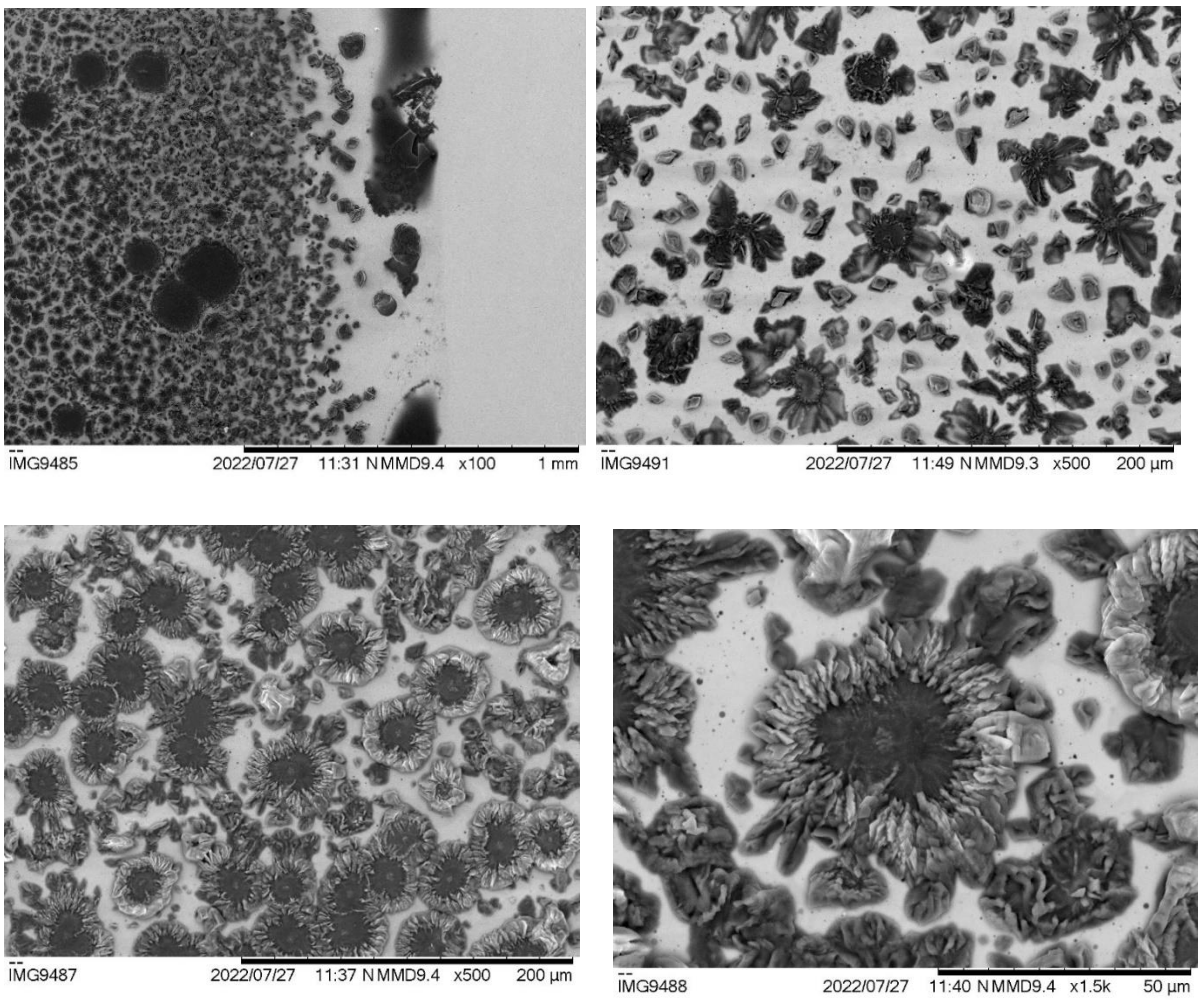

Appendix A.3- SEM imagery of electrodeposited MnO_2 thin films:
100X magnification(top-left); 500X magnification (top-right); 500X magnification (bottom-left); 1500X magnification (bottom-right)

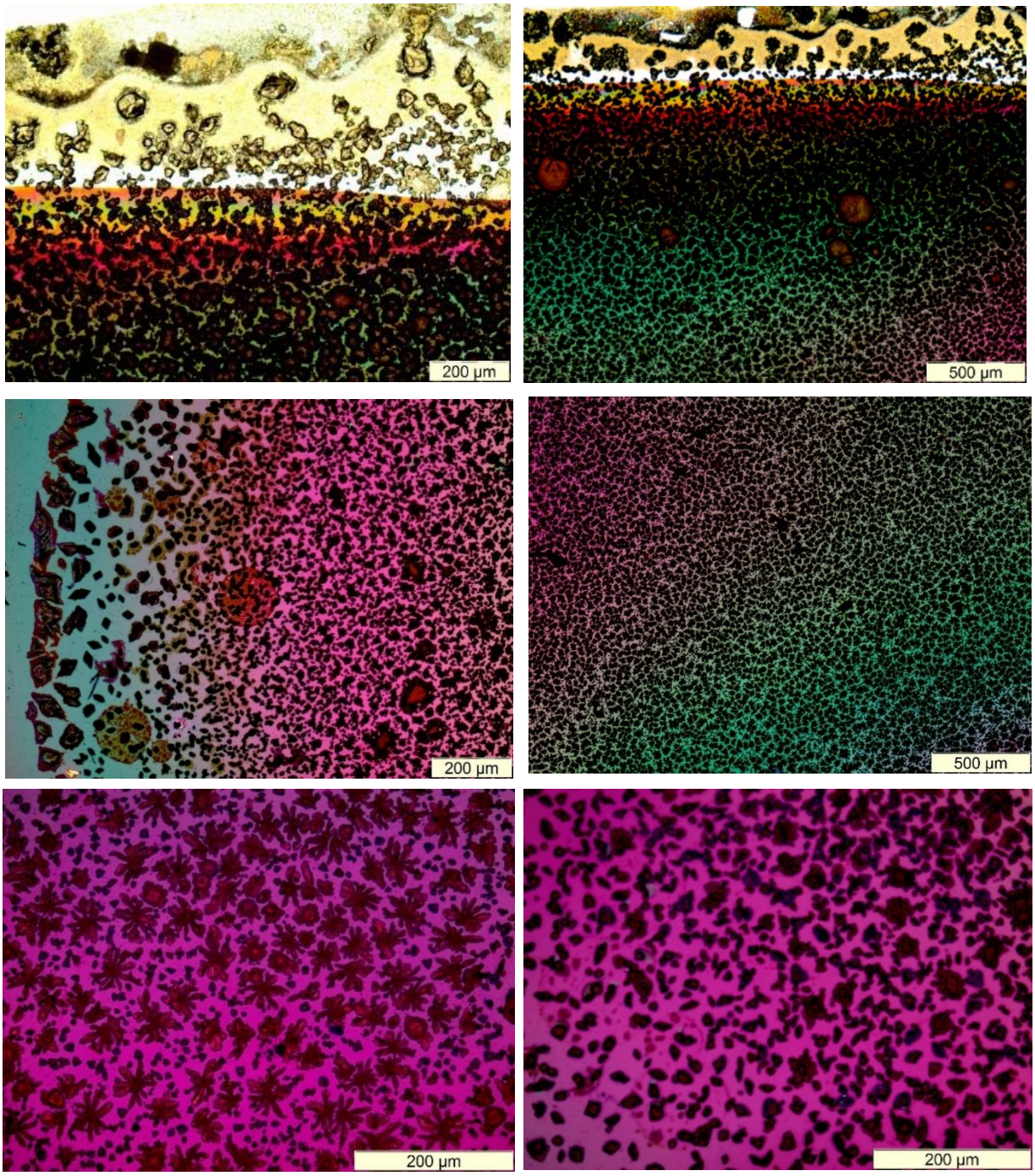

Appendix A.3- Bright-field mode OM Images of MnO_2 films.